



Back to Single-carrier for beyond-5G communications above 90 GHz

Grant agreement ANR-17-CE25-0013

## Deliverable D2.0

# Propagation channel model and RF impairments definition

<b>Delivery date</b>	21/02/2019
<b>Version</b>	1.0
<b>Editor</b>	Yoann Corre (Siradel)
<b>Authors</b>	Siradel: Yoann Corre, Grégory Gougeon CEA-Leti: Simon Bicaïs, Jean-Batiste Doré
<b>Dissemination</b>	Public
<b>Keywords</b>	Tbps, Beyond 5G, Channel modelling, RF impairments modelling

### History

Version	Date	Modification	Author(s)
1.0	21/02/2019	First version	Y. Corre

## Executive summary

This deliverable gives a state-of-the-art and first BRAVE outcomes related to the characterization and modelling of the sub-THz physical layer (above 90 GHz). This will serve the identification of appropriate radio modulation schemes and efficient waveforms for sub-THz beyond-5G communications; and will contribute to the performance assessment in terms of coverage range, throughput, capacity, signal processing complexity and power consumption.

First, the Deliverable D2.0 explores the wireless channel properties inside a typical office building, for ranges up to 20 meters, in line-of-sight (LoS) and non-line-of-sight (NLoS) situations. The path-loss, delay spread, angular spread and coherence bandwidth are evaluated based on ray simulations. The channel properties in frequency range 90 to 200 GHz are compared to those simulated in same conditions at 2 GHz or within the 5G millimetre-wave spectrum. The path-loss and the channel spreading parameters are severely affected by the presence of obstructing partitions, but the reflections remain a very powerful propagation mechanism. Actually, a major factor that impacts the wireless channel is the antenna beam-width. The channel is observed to be “flat” over a 100 MHz bandwidth or even wider, when the beam-width at one terminal is 6°.

A similar analysis is conducted for lamppost-to-lamppost links (up to 200 meters range) in an urban outdoor scenario. The results are representative of the physical channel that would be experienced by a sub-THz mesh xhaul infrastructure feeding a dense small-cell access network or a fixed wireless access (FWA) infrastructure. The antenna beam-width at each terminal is supposed to be thin enough such that only the dominant path is captured. The blockage by buildings plays obviously the major role. But the attenuation by trees is another critical propagation component; it is simulated based on accurate 3D representation given by LiDAR point clouds technology. A path-loss exponent between 2.3 and 3.0 is observed in situations where the direct link is obstructed by some vegetation. The exact value of the path-loss exponent varies with the vegetation loss that is considered, which actually depends on branch and leave density. Today, the appropriate values for sub-THz vegetation loss remain unknown.

Both the in-office and outdoor wireless simulations are synthesized into approximate analytical models, where the path-loss and spreading properties are only depending on very few parameters. However simplified, such models are often convenient for integration of the physical layer into link or system-level studies.

Second, the Deliverable D2.0 investigates the generation of phase noise in oscillators and its effect on the communication systems performance. As the frequency increases, the phase noise becomes stronger, and its mitigation more complex. A sub-THz phase noise model is proposed beyond the current state-of-the-art (i.e. Gaussian, Wiener and Leesson models). Phase noise is modelled as the sum of a frequency-flat (or white) component partly due to the reference crystal and several coloured components from the free-running oscillator that respectively depends on  $1/f^3$ ,  $1/f^2$ ,  $1/f$  and  $f_0$ . Below the nominal bandwidth  $\gamma$  of the PLL (Phased Locked Loop), the phase noise by the crystal prevails and is referred to as the near-carrier phase noise, while above the cut-off frequency  $\gamma$ , the VCO (Voltage Controlled Oscillator) is the main contribution. This model is derived into a versatile simulation architecture, which may be directly

calibrated upon oscillator spectral measurements. The choice of the phase noise model depending on the oscillator spectral properties and application will be investigated later in BRAVE project.

Today, the mathematical convenience of the phase noise Gaussian model is exploited to represent the poor performance of sub-THz systems, to optimize constellations and to improve the demodulation performance. An optimized sub-THz demodulator is derived for M-QAM modulations when high-SNR (Signal-to-Noise Ratio) signal is corrupted by gaussian phase noise. The symbols modulation and the optimal demapper are defined using polar metrics instead of the traditional I/Q metrics. The polar metrics are shown to greatly enhance the performance of coded systems. The optimal signal processing as well as some performance assessments are given.

The research and conclusions reported in this document will be completed in future deliverable D2.1 that is due in mid-2020. This future BRAVE delivery will provide deeper analysis of the physical layer, along with further description and evaluation of the proposed modulation schemes and waveforms.

# Table of content

<b>1</b>	<b>INTRODUCTION .....</b>	<b>6</b>
<b>2</b>	<b>PROPAGATION CHANNEL MODELLING.....</b>	<b>8</b>
2.1	REQUIREMENTS .....	8
2.2	STATE-OF-THE-ART .....	8
2.3	BRAVE RESEARCH .....	13
2.4	EXTENSION AND TEST OF THE RAY-BASED SIMULATOR .....	13
2.5	IN-OFFICE SCENARIO .....	17
2.5.1	<i>Description.....</i>	<i>17</i>
2.5.2	<i>Simulation results.....</i>	<i>19</i>
2.6	IN-STREET SCENARIO .....	25
2.6.1	<i>Description.....</i>	<i>25</i>
2.6.2	<i>Simulation results.....</i>	<i>26</i>
2.7	PERSPECTIVE.....	28
<b>3</b>	<b>RF IMPAIRMENTS MODELLING.....</b>	<b>29</b>
3.1	INTRODUCTION .....	29
3.2	PHASE NOISE IN OSCILLATORS.....	30
3.2.1	<i>Ideal vs noisy oscillators.....</i>	<i>30</i>
3.2.2	<i>Noise sources .....</i>	<i>31</i>
3.2.3	<i>Phase noise generation mechanism .....</i>	<i>31</i>
3.2.4	<i>Phase noise spectrum.....</i>	<i>32</i>
3.3	IMPACT OF PHASE NOISE IN COMMUNICATION SYSTEMS .....	33
3.3.1	<i>Communication system model.....</i>	<i>33</i>
3.3.2	<i>Capacity of the phase noise channel .....</i>	<i>34</i>
3.4	REALISTIC PHASE NOISE MODEL AND SIMULATION .....	36
3.4.1	<i>Proposed model .....</i>	<i>36</i>
3.4.2	<i>Simulation.....</i>	<i>37</i>
3.5	CONCLUSION AND FUTURE WORK.....	39
<b>4</b>	<b>APPLICATION: OPTIMUM DEMODULATION IN THE PRESENCE OF GAUSSIAN PHASE NOISE</b>	<b>40</b>
4.1	INTRODUCTION .....	40
4.2	SYSTEM MODEL.....	40
4.2.1	<i>Channel.....</i>	<i>40</i>
4.2.2	<i>Phase noise.....</i>	<i>41</i>
4.3	MAXIMUM LIKELIHOOD SYMBOL DETECTION.....	41
4.3.1	<i>Optimum decision metric at high SNR .....</i>	<i>41</i>
4.3.2	<i>Framework.....</i>	<i>43</i>
4.3.3	<i>Application: demodulation of uncoded M-QAM.....</i>	<i>44</i>
4.4	PROBABILISTIC DEMAPPER.....	44
4.4.1	<i>Bit LLR (Log Likelihood Ratio) values.....</i>	<i>44</i>
4.4.2	<i>Application: demodulation of LDPC coded M-QAM.....</i>	<i>46</i>
4.5	CHANNEL ESTIMATION FOR OPTIMAL DEMODULATION .....	46
4.5.1	<i>Thermal and phase noise variances estimation .....</i>	<i>47</i>
4.6	CONCLUSION.....	48
<b>5</b>	<b>CONCLUSION .....</b>	<b>49</b>
	<b>REFERENCES.....</b>	<b>50</b>
	<b>APPENDIX A – IN-OFFICE SCENARIO CDF RESULTS.....</b>	<b>54</b>

## List of Acronyms

<b>5G</b>	5th Generation
<b>AWGN</b>	Additive White Gaussian Noise
<b>B5G</b>	Beyond 5G
<b>BER</b>	Bit Error Rate
<b>BW</b>	Bandwidth
<b>CDF</b>	Cumulative Distribution Function
<b>CPE</b>	Customer Premises Equipment
<b>CSI</b>	Channel State Information
<b>DL</b>	Down Link
<b>EPL</b>	Excess Path Loss
<b>FWA</b>	Fixed Wireless Access
<b>LDPC</b>	Low Density Parity Check
<b>LIDAR</b>	Light Detection and Ranging
<b>LLR</b>	Log Likelihood Ratio
<b>LoS</b>	Line-of-Sight
<b>LTI</b>	Linear Time Invariant
<b>MIMO</b>	Multiple Inputs Multiple Outputs
<b>ML</b>	Maximum Likelihood
<b>mmWave</b>	Millimeter-wave
<b>MVUE</b>	Minimum Variance Unbiased Estimator
<b>NPA</b>	Non linear Power Amplifier
<b>NLoS</b>	Non LoS
<b>OTFS</b>	Orthogonal Time Frequency Space
<b>PLE</b>	Path Loss Exponent
<b>PLI</b>	Path Loss Intersect
<b>PLL</b>	Phase Locked Loop
<b>PN</b>	Phase Noise
<b>PSD</b>	Power Spectral Density
<b>QAM</b>	Quadrature Amplitude Modulation
<b>RF</b>	Radio Frequency
<b>SEP</b>	Symbol Error Probability
<b>SNR</b>	Signal to Noise Ratio
<b>Tx</b>	Transmitter / Transmit
<b>UE</b>	User Equipment
<b>UL</b>	Up Link
<b>VCO</b>	Voltage Controlled Oscillator

# 1 Introduction

This Deliverable describes two major components of the communication systems physical layer, along with their particularities at sub-THz frequencies: 1) the wireless propagation channel, and 2) the random phase noise generated by oscillators. The preliminary outcomes of the BRAVE research are reported, which aim at extending the state-of-the-art models to frequencies above 90 GHz. The derivation of an optimal modulation-demodulation scheme that optimally operates in presence of a strong phase noise is presented as well.

The proposed models must apply to the main sub-THz scenarios identified in Deliverable D1.0: short-range communications, kiosk, mobile access in hotspots, fixed back- or front-haul. The considered BRAVE waveforms are transmitted in highly wide channel bandwidths (several hundreds of MHz) to provide ultra-high capacity with enhanced energy efficiency.

One BRAVE objective is the definition of a multi-path wireless propagation channel model that is appropriate for frequency bands between 90 and 200 GHz. Similar to the mmWave channel that is intensively measured and simulated today in the 5G context, the sub-THz channel is expected to be scarce i.e. composed of only few dominant paths, typically the line-of-sight contribution, one-bounce specular reflections (from electrically-large surfaces) and possible discrete scattering (from objects with small electrical size). The properties of diffuse components (from foliage or façade details) are under investigation by the scientific community but is still not precisely known. The masking effect by the vegetation (foliage and trunk), small objects (e.g. urban furniture, cars, bodies) or façade details plays a major role in the channel properties that also needs for better characterization and modelling.

The Siradel approach, which is considered in the BRAVE project, relies on a deterministic ray-based simulation (Volcano software). The model supports all possible in-building and urban scenarios, and may be enhanced with stochastic components to account for dynamic and/or small objects. It is extended to the sub-THz domain by introducing new material properties and appropriate gas attenuation. It is also enhanced in order to detect obstruction and vegetation penetration length from laser 3D point cloud data. The resulting Volcano prototype is exploited in two channel characterization studies, first inside a typical office environment, second for urban street-level xhaul links. Many ray-based simulations are conducted in each environment. Their analysis gives statistics on the path-loss versus distance. The in-office scenario is exploited into a deeper manner, along with characterization of the delay spread, angular spread and coherence bandwidth for different antenna beam-widths.

This wireless channel characterization is reported in Section 2.

For practical system designs and realistic performance evaluations, hardware impairments from the radio frequency (RF) chains should be considered adequately. Several hardware aspects need to be modelled to enable simulations, including phase noise (PN), non-linear power amplifiers (NPA), and I/Q imbalance. Proper modelling of these imperfections at sub-THz range is of special importance and is required to study the resulting performance degradation in different channel scenarios. In this document, the focus is

put on the characterization and modelling of the phase noise, which is of critical importance in sub-THz domain, while usually neglected at lower frequencies. It is expected to strongly degrade the traditional modulation-demodulation schemes. Therefore accurate modelling is required to assess this performance degradation and elaborate new approaches.

Section 3 explains the various causes for phase noise, and gives a state-of-the-art on the literature models. An original and more realistic high-frequency model is described, along with the associated simulation architecture.

Finally, a new modulation and detection scheme is proposed in Section 4 that is optimal under Gaussian phase noise and high signal-to-noise ratio. The enhanced detector structure relies on the use of polar metrics. The required signal processing (demapper and channel estimation) is exposed, while the performance under various phase noise intensities is assessed.

A short conclusion and perspective are drawn in Section 5.

## 2 Propagation channel modelling

### 2.1 Requirements

Deliverable D1.0 [1] defined B5G scenarios and requirements to be assessed through simulation. Some scenario parameters impact the radio propagation channel and have to be taken into account in the channel modelling. Indoor or outdoor environment has to be described for a precise prediction of the LoS or NLoS condition, the coverage range and the multipath properties of the channel. Environment mobility such as people or moving vehicles is of importance at the frequencies of interest because it can lead to untimely signal blockage. Also, because the coverage range must be leveraged with high gain directional antennas, more precisely with beamforming from antenna arrays, the trade-off between gain and directivity must be analysed through the channel properties.

### 2.2 State-of-the-art

The properties of the radio wave propagation in the 90-200 GHz band are not properly known, and no channel model (deterministic or stochastic) has been formally validated and recognized by the scientific community yet. The characteristics of the propagation channel and its modelling are nevertheless critical inputs for several research tasks: definition of adequate scenarios (cell range, supported propagation environments), elaboration of PHY-layer algorithms (e.g. waveform, channel estimation, equalization), evaluation and refinement of multi-antenna systems, link- and system-level simulations.

The scientific propagation community is today producing intensive activity on the mmWave bands that are envisaged for future 5G. It includes backhauling and access solutions, both indoor and outdoor environments, considering large-bandwidth and high antenna directivity. Propagation in those bands is characterized by very strong obstruction losses due to the frequency itself ( $1/f^2$  power decrease in free space) and the impact of the environment, for which ITU provides some recommendations which are enumerated below.

Figure 1 shows the propagation loss caused by atmospheric gases [2]. After the well-known peak at 60 GHz, the loss keeps increasing with another peak of almost 30 dB/km at 185 GHz, which is in the scope of BRAVE. The atmospheric attenuation remains irrelevant in short-range scenario such as kiosk or hotspot, but is of particular importance for backhaul links where the distance can be larger than 100 m up to a few kilometres.



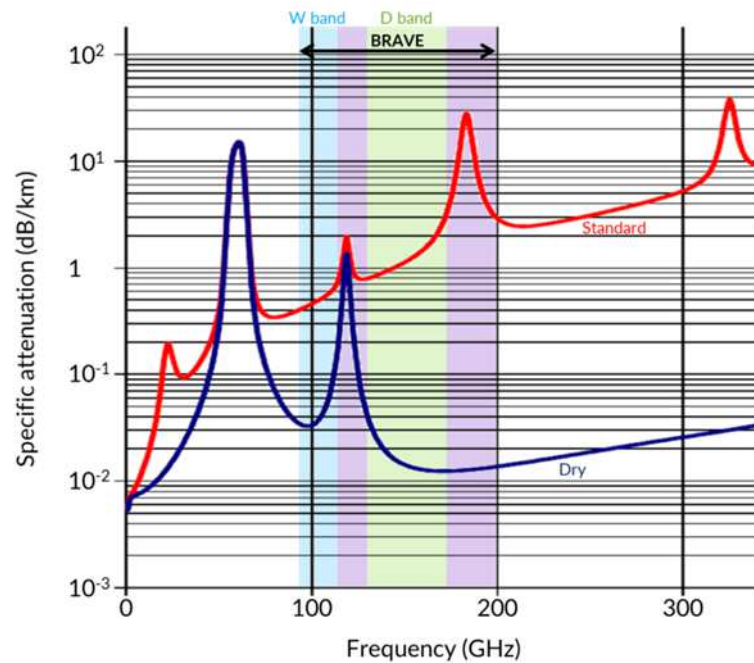


**Figure 1: Attenuation by atmospheric gases, modified version of a graph given in [2]**

Figure 2 shows the attenuation due to the rain modelled by a curve-fitting to power-law coefficients derived from scattering calculations [3]. It is rapidly increasing up to 100 GHz, but reaches a plateau, and then is almost constant at higher frequencies. Indoor and short range scenarios are not impacted. However when it comes to the backhaul links, especially when the distance is a few hundreds of meters or even a few kilometres, transmissions are affected. The rain attenuation must be taken into account in the link budget with a margin that assures the target backhaul availability e.g. 99.9%.

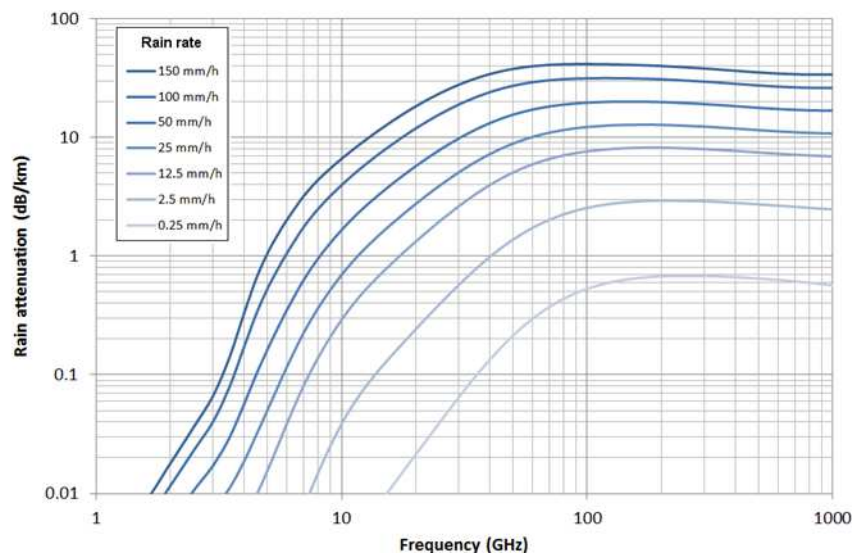


**Figure 2: Rain attenuation**

Figure 3 shows the attenuation due to the vegetation up to 30 GHz, which raises up to some dB/m [4]. If we assume it can be extrapolated, the attenuation is expected to be 40 dB/m at 200 GHz, making any

small vegetation intersection a blocking obstruction for the signal. This is of much critical importance for the outdoor hotspot, backhaul and FWA scenarios. This obviously impacts the coverage of the hotspots, with possibly a deep shadow behind the trees. We may as well expect strong and rapid fading, which requires resilient communication systems and protocols, i.e. based on dual-connectivity. The design of a sub-THz cell or sub-THz link will require great attention at the vegetation representation, and propagation modelling. Assessment of the vegetation loss, which actually depends on the frequency, branch/leaf density, and humidity, is a complex topic that need for a large amount of field measurements. As they may offer an alternative to the obstructed direct propagation path, the reflections on the ground and building façades have to be computed. SIRADEL has enhanced its ray-based propagation model in order to support a fine description of the vegetation, thanks to LiDAR point cloud, and make this compatible with multi-paths. This is investigated, prototyped and tested in scope of BRAVE spectrum. See section 2.6.1 for more details.

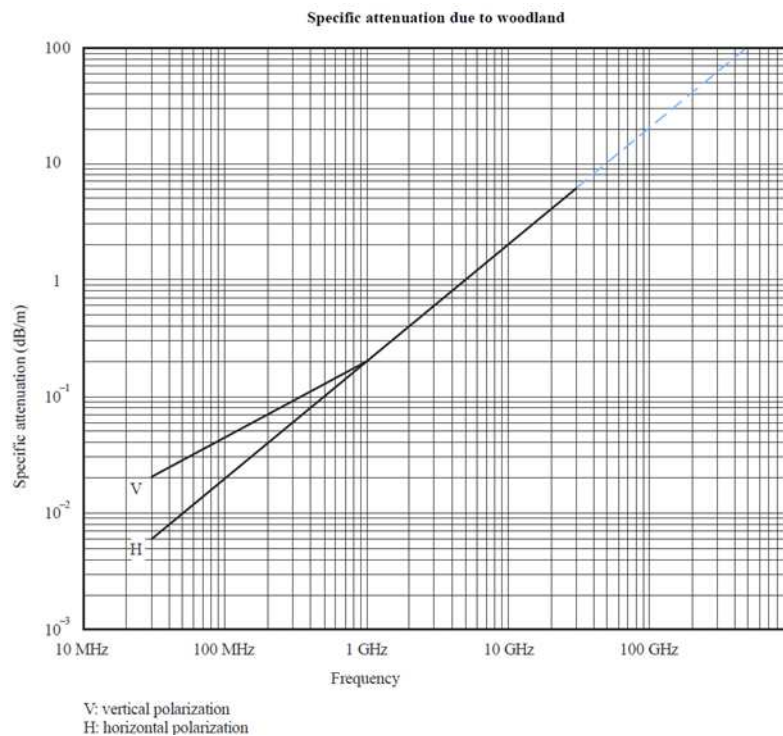


**Figure 3: Vegetation attenuation, modified version of a graph given in [4]**

The Building Entry Loss (BEL) or indoor penetration loss is now commonly characterized for two different categories of building (Figure 4): traditional, or thermally-efficient [5]. The latter category generally applies to recent (or renovated) office buildings with modern glasses having a specific protection against sun radiation. The median penetration loss at 100 GHz is predicted to be 23.9 dB in the traditional buildings, and 56.1 dB in the thermally-efficient buildings. We may consider the building façade is providing quasi-full isolation for radio propagation in sub-THz spectrum. This prevents for outdoor-to-indoor and indoor-to-outdoor communication scenarios, and limits the interference between cells separated by a façade.

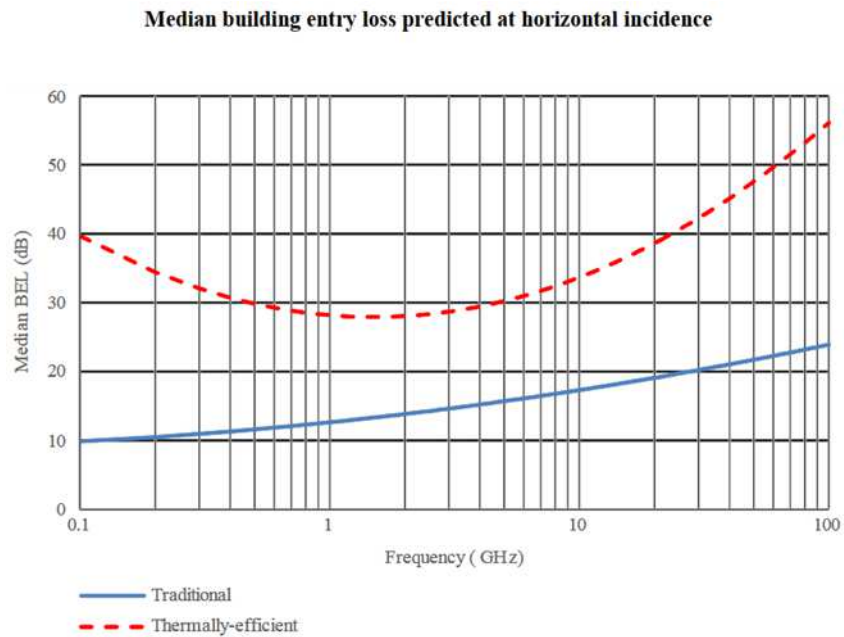


**Figure 4: In-building penetration loss [5]**

Both the building entry loss and the in-building propagation are affected by strongest attenuation through the building materials. As well as the building external façade, the internal walls and doors are creating isolated rooms. Sub-THz material characterization was quite limited in previous decades, as the main research was focussed on lower frequencies. However the scientific community's interest is moving. In [6] and [7] the transmission loss of typical indoor materials such as plasterboard walls, clear glass, closet door or steel door are measured at 28 GHz and 73 GHz respectively by the New York University (NYU). More recently, NYU started the same measurements at 140 GHz [8]. Figure 5 is a summary of these three measurement campaigns results for drywall and clear glass samples. NYU plans more measurement at 140 GHz at the same locations as the 28 and 73 GHz campaigns to complete the comparison table.

Frequency (GHz)	MUT	Thickness (cm)	Penetration Loss (dB)	Avg. Penetration Loss (dB/cm)
28 [1], [45]	Clear glass A	1.2	3.6	3.0
28 [1], [45]	Clear glass B	1.2	3.9	3.25
28 [1], [45]	Drywall A	38.1	6.8	0.18
73 [44]	Clear glass C	0.6	7.72	12.87
73 [44]	Clear glass D	0.6	7.1	11.83
73 [44]	Drywall B	14.5	10.06	0.73
140	Clear glass C	0.6	8.24	13.73
140	Clear glass D	0.6	9.07	15.12
140	Glass door (Front door)	1.3	16.2	12.46
140	Drywall B	14.5	15.02	1.04
140	Drywall with Whiteboard	17.1	16.69	0.98

**Figure 5: Comparison of drywall and clear glass penetration loss at 28, 73, and 140 GHz [8]**

Sparse propagation channel is generally observed in mmWave bands, where the line-of-sight (LoS) direct-path is the most dominant component. Many propagation paths that bring significant power at a lower frequency are either attenuated by obstacles or suffer from some interactions weakness

(diffraction, diffuse scattering). That is still true in sub-THz spectrum, and might even be slightly amplified. Nevertheless, some specular strong contributions are still present, leading to a few propagation clusters, along with significant delay and angular spreading. Main contributors are reflections on flat surfaces as walls, floor, or windows. Because the wavelength is lower than 3 mm, small objects in particular metallic objects may also cause a significant echo due to a reflection or scattering.

Remark that the channel sparsity is further increased by the use of highly-directive antennas, which will compensate for global higher path-loss at sub-THz frequencies. Some multi-paths transmitted and/or received out of the antennas beamwidth are filtered out. This effect has been captured by [9] where the 60-GHz delay and angular spreads do depend on the antenna beamwidth (Figure 6). Recommendations [9] and [10] propose a beamwidth-dependent model for different scenarios at 28 and 38 GHz in respectively indoor and outdoor environments.

Frequency (GHz)	Tx antenna	Rx antenna beamwidth (degrees)	Static r.m.s. delay spread (90 <sup>th</sup> percentile) (ns)	Room size (m)	Remarks
60	Omnidirectional	Omnidirectional	17	13.5 × 7.8	Ray-tracing
		60	16	Empty office room	
		10	5		
		5	1		
		Omnidirectional	22	13.0 × 8.6 Empty office room	Ray-tracing NLoS
		60	21		
		10	10		
		5	6		

**Figure 6: Example of antenna directivity dependence of static r.m.s. delay spread [9]**

Only few scientific publications report today on channel characterization above 90 GHz. [11] describes and analyses few channel sounding measurements in a shopping mall at 28 and 140 GHz. Similar delay spreads and angular spreads are found in both frequency bands. Paper [12] reports on indoor measurements in bands V (60 GHz), E (70 – 80 GHz) and D (126 – 146 GHz). The delay spread is found to be lower in the D-Band. Even if similar propagation paths can be identified in each band, the longest echoes are not detected in the D-band (possibly due to limitation in the measured power dynamic). Paper [13] presents a large set of measurements in several bands up to 86 GHz with a focus on delay spread also. The conclusion is that delay spread does not vary much with frequency.

The channel stationarity or non-stationarity over the signal bandwidth and antenna array have a major impact on the system performance. Multi-link spatial consistency is another key feature that must be properly predicted for addressing ultra-dense small-cell networks or multi-user connectivity, but needs complex modelling. The geometry-based stochastic models as WINNER+, METIS, mmMAGIC, MiWEBA or 3GPP offer convenient solutions; they do already address the frequencies above 6 GHz, up to 100 GHz in some cases. New propositions are regularly made to refine the stochastic parameters or model structures, based on channel sounding measurements. To the best of our knowledge, there is no extension towards the sub-THz frequencies yet.

Besides, the ray-based deterministic simulators (using geographical representation), which were mainly devoted to radio-planning before, are today considered as a valuable tool able to reproduce all or part of the expected sparse channel characteristics in mmWave band. They may generate channel samples for link or system simulations, or may be hybridized with stochastic processes as proposed in the 3GPP, MiWEBA or mmMAGIC models. The basics of those simulators are compliant with higher frequencies, thus can be applied in sub-THz domain. Adjustments are required, which are further discussed below.

## 2.3 BRAVE research

The derivation of a channel model compliant with frequencies above-90 GHz is done under the leadership of SIRADEL, expert in propagation simulation for more than twenty years. SIRADEL edits a ray-based solution that is regularly enhanced and was recently adjusted by comparison to outdoor measurements up to 80 GHz. Hybridation with stochastic components is another active research topic at Siradel e.g. for human body obstruction. In BRAVE, the effort will be extended towards frequencies in the range 90 – 200 GHz. The main structure of the deterministic simulator is expected to be still valid (construction of multi-paths, reflection and diffraction coefficients), however many extensions will be required, including: refinement of the material properties; impact of the rainfall and gas absorption; vegetation modelling (critical for obstructed line-of-sight propagation in outdoor environment); prediction of the frequency non-stationarity for envisaged huge bandwidths; prediction of the spatial channel consistency, including fading at different scales; and human body blockage. The accuracy of the environment's representation e.g. foliage, small objects, or details of a building façade, is a critical element which may lead to major local fluctuations.

This work is achieved by combining literature survey with ray-based simulations in a few scenarios of interest in BRAVE project.

This will lead to the following outcomes:

- Characterization of the main channel properties in the sub-THz spectrum, i.e. path-loss versus distance, delay spread, angular spread and frequency coherence.
- Simulation of channel samples for elaboration and/or evaluation of proposed BRAVE innovation.
- Determination of the connectivity range and performance.
- Demonstration of proposed BRAVE applications.

This work is conducted in hotspots and urban backhauling scenarios. The implemented innovations and first characterization studies are reported in following sub-sections.

## 2.4 Extension and test of the ray-based simulator

The ray-based engine that is used to create the sub-THz prototype simulator has been successfully employed for more than 15 years in the sub-6 GHz band, and has already been experienced in the past few years in the mmWave domain up to 80 GHz [14]. The tool is either applied on small-scale scenarios (trademark VolcanoFLEX) or large-scale urban scenarios (trademark VolcanoURBAN), embedded into commercial software devoted to the wireless network design or propagation channel prediction. The main evolutions that have currently been implemented are two-fold:



1. Extension of the EM material properties library up to 200 GHz.
2. Management of highly detailed representation of the environment, from LiDAR point cloud.

### Extension of the materials library

The original simulator relies on the definition of materials permittivity and conductivity, in particular those given in [15 – Table 3] for frequencies up to 100 GHz. To the best of our knowledge, there is no yet any achieved global action for summarizing material's properties in the sub-THz spectrum, mostly because the interest in those frequencies is very recent. Therefore, we decided to simply consider the ITU models at 100 GHz and extend their application up to 200 GHz. The relative permittivity is constant versus frequency, while the conductivity varies as  $f^d$  with  $d$  in range [0; 1.4].

The implementation was validated by test simulations that assess the transmission, reflection and diffraction coefficients from four following materials: glass, concrete, plasterboard and wood. In particular, Figure 7 shows the transmission loss as a function of the frequency and material's width. The plasterboard that is almost transparent below 6 GHz leads to more than 20 dB loss over most part of the BRAVE spectrum. Concrete walls are fully opaque above 60 GHz. Outdoor-indoor isolation is thus expected in BRAVE bands as well as room isolation in indoor environment.

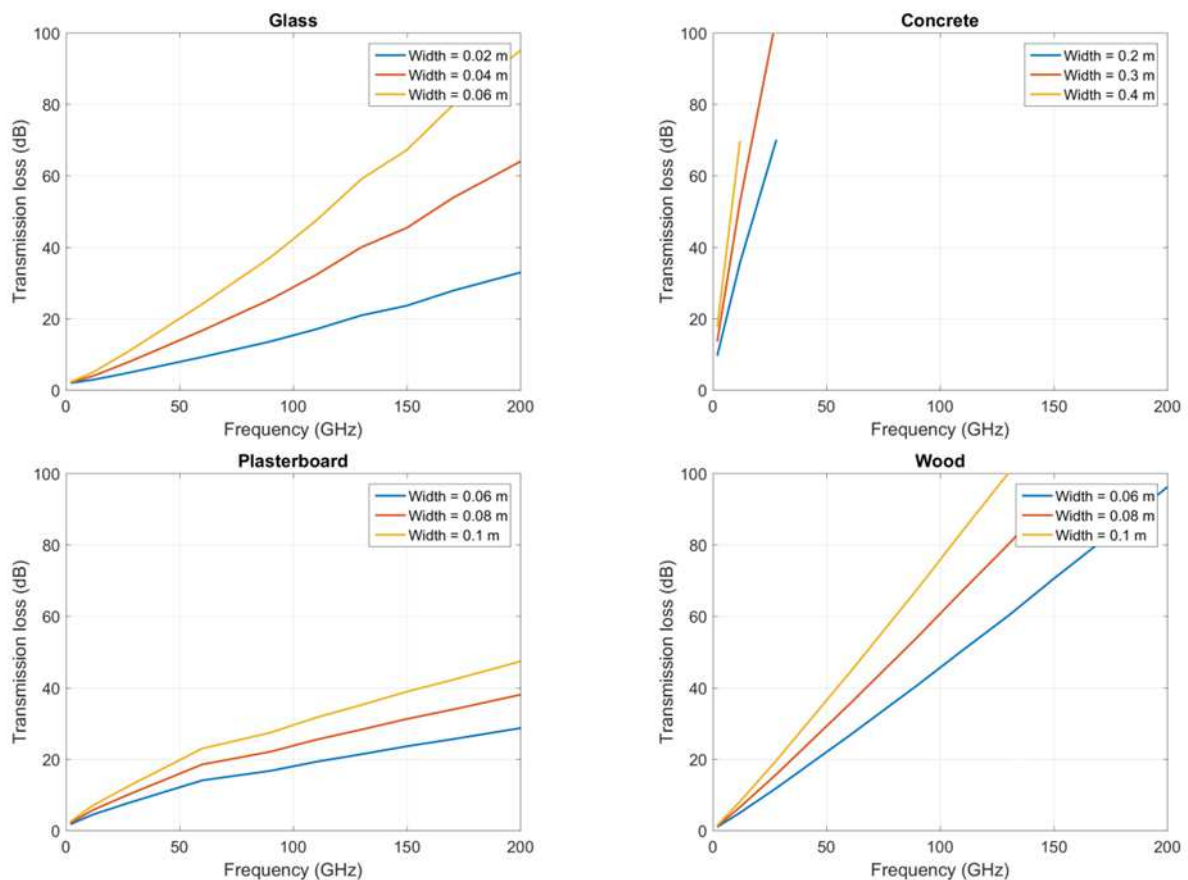
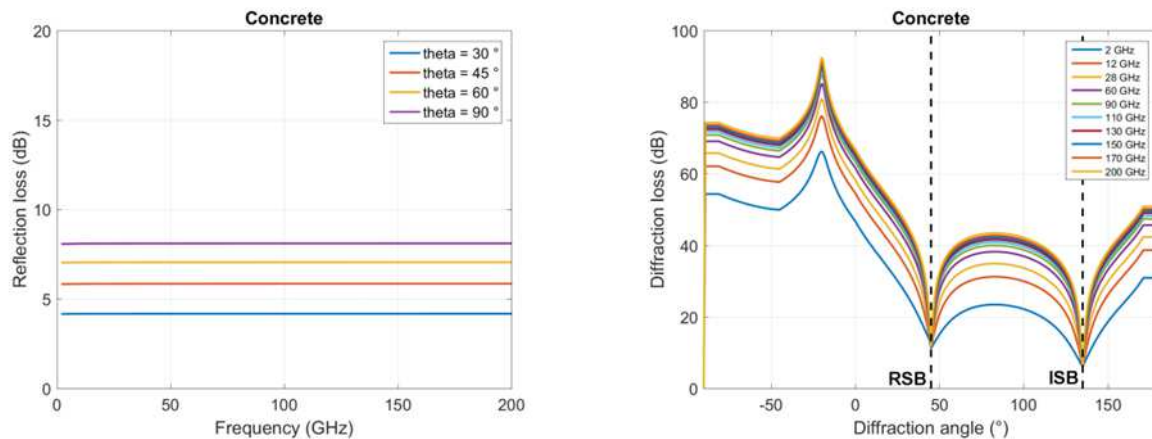


Figure 7: Transmission loss of typical materials

Figure 8 shows the reflection loss for a 20 cm large concrete wall and the diffraction loss for a 90° concrete corner with 45° incident wave. The reflection loss is constant with frequency, which was expected. The simulated reflected paths will be as strong in sub-6GHz, mmWave and BRAVE sub-THz spectrum. On the contrary, the diffraction loss is roughly 20 dB at 200 GHz compared to 2 GHz, except for specific angles in vicinity of RSB and ISB, respectively the reflection and incident shadow boundaries. Other materials show very similar behaviours.



**Figure 8: Reflection and diffraction losses of concrete**

### Management of LiDAR point cloud data

The VolcanoURBAN tool predicts the propagation loss above the clutter based on the well-known knife-edge diffraction technique (including some heuristics). 3D multiple paths are created from a ray-launching process: reflections on the building façades, diffraction at the building edges, or reflection on the ground, possibly combined with above-clutter propagation. Based on recent research activity, the tool was adjusted and validated in several mmWave frequency bands, from 28 to 80 GHz. More particularly, the way to manage the vegetation obstacles has been improved [16]. Both the transmission through the vegetation and the diffraction on bottom and top of the foliage are considered. The transmission is computed from an average linear loss (dB/m) that is multiplied by the propagation length inside the foliage. The resulting model cannot precisely compute the strong and rapid fading that is experienced behind an obstructing tree or group of trees, but gives an estimate of the average shadowing.

The VolcanoURBAN technology traditionally handles raster and vector geographical representations, as shown in Figure 9 (a) and (b), but it has been enhanced to also support LiDAR point cloud data (c). Therefore the mmWave and Sub-THz computation can take benefit of a far more accurate representation of the vegetation (real 3D shape) for blockage detection and estimate of the transmission depth.

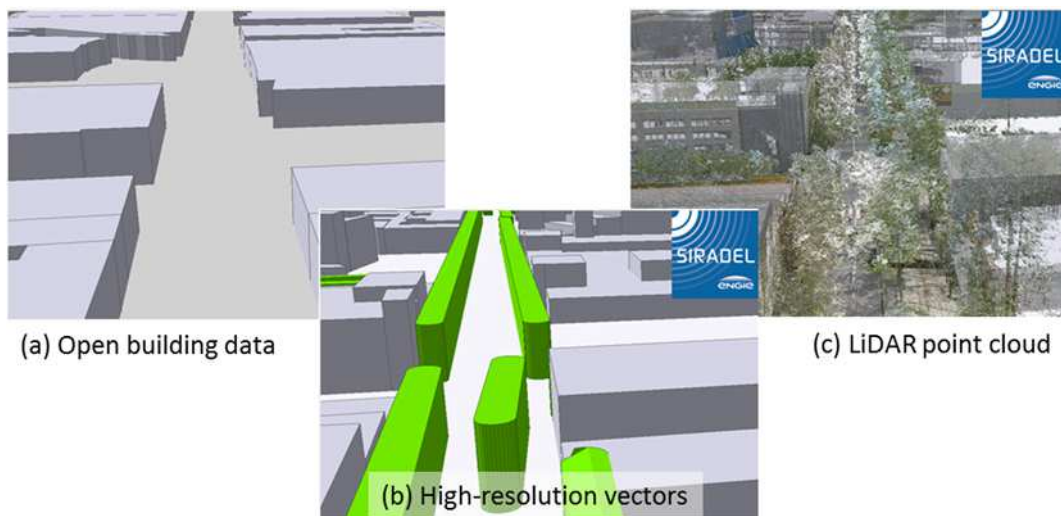


**Figure 9: Geo map data for urban simulation**

Figure 10 shows an example of vegetation blockage as seen in the direct vertical profile of a 94m-long link. LiDAR-based computing consumes more memory, calculation and time. Nevertheless the implementation has been optimized such that it remains compatible with common computer capabilities and requires only a very few seconds computation per link, even when multi-paths are activated.

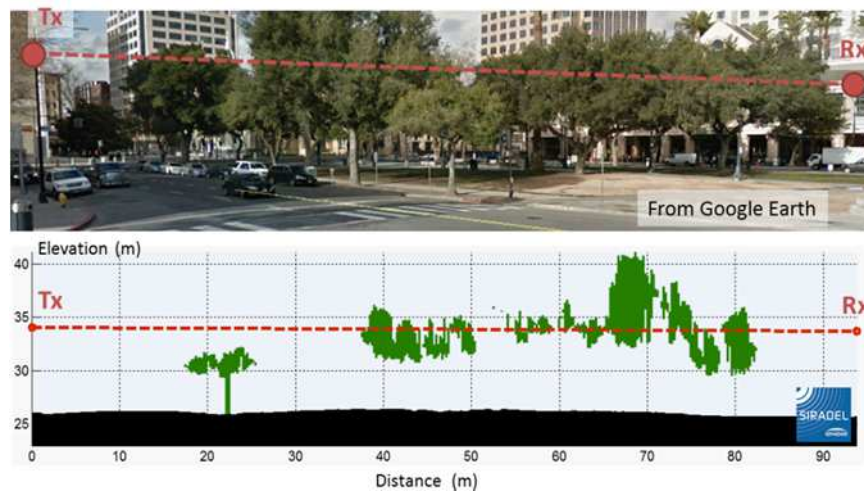


**Figure 10: Extraction of the vertical profile from the point cloud data**



The point cloud information is exploited for computation of all multiple paths due to interaction with buildings, vegetation and ground, as illustrated in Figure 11.



**Figure 11: Example of a LiDAR-based multi-path channel simulation**

After validation, the sub-THz prototype has been employed in two separate scenarios for in-office and urban street-level channel characterization, as detailed in following sections.

## 2.5 In-office scenario

The work that was conducted in the office scenario leads to the generation of multi-channel samples, and a statistical analysis of the channel properties at different frequencies.

### 2.5.1 Description

The considered environment is depicted in Figure 12; it is a typical single-floor office of size 20 m x 10 m as described in [17]. It is composed of external walls, windows, internal walls, cubicle partitions (2 meters high) and desks. The propagation channel is computed from 10 different access points, which are installed at realistic locations i.e. on the wall or below the ceiling at 2.5 m height. 50 user locations at 1.5 m height are computed; they are distributed in the different rooms of the building. All possible 500 links between the access points and the user locations are predicted, aiming at a statistical overview of the channel properties in this environment.

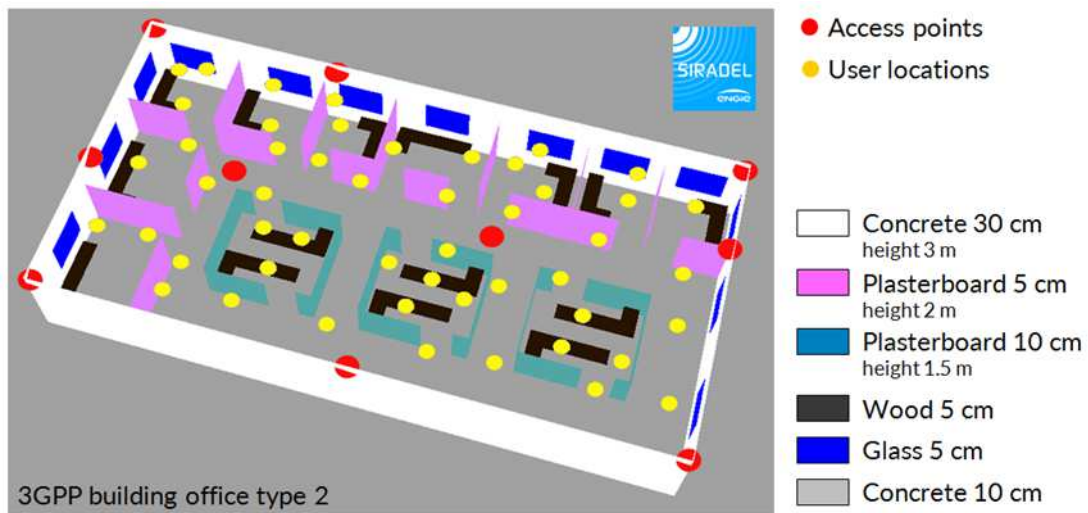


**Figure 12: In-office scenario environment**

The ray tracing model enables to predict multiple paths as shown in Figure 14, where some reflected paths (on the ground and ceiling) bring as strong contributions as the obstructed direct path.

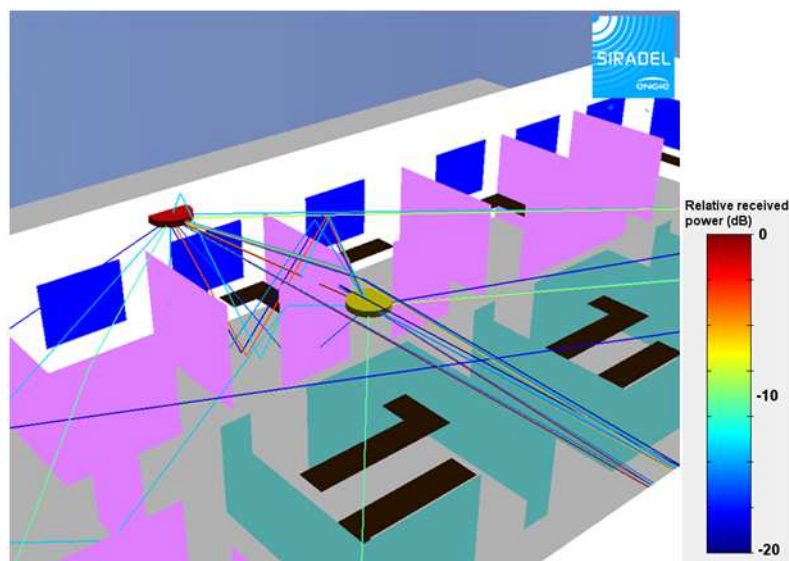


**Figure 13: Multiple indoor paths**

The 500 links are predicted in three different conditions:

- Access points equipped with an isotropic antenna
- Access points equipped with a 20°-beamwidth antenna (Figure 14, left)
- Access points equipped with a 6°-beamwidth antenna (Figure 14, right)

These three simulations aim at comparing the channel properties as a function of the antenna beamwidth. The 20° and 6°-beamwidth radiation patterns are representative of a beamforming antenna system, which is foreseen to be mandatory on in sub-THz communication in order to focus the energy towards the user, and thus benefit from better gain. In our study, the beam of the access point is automatically oriented towards the best propagation path (either direct or indirect).

In all three cases, the EIRP is 0 dBm and the user is equipped with an isotropic antenna.

The simulations are performed at the following frequencies: 2, 12, 28, 60, 90, 110, 130, 150, 170 and 200 GHz in order to observe the channel evolution from medium cellular frequency bands to BRAVE sub-THz.

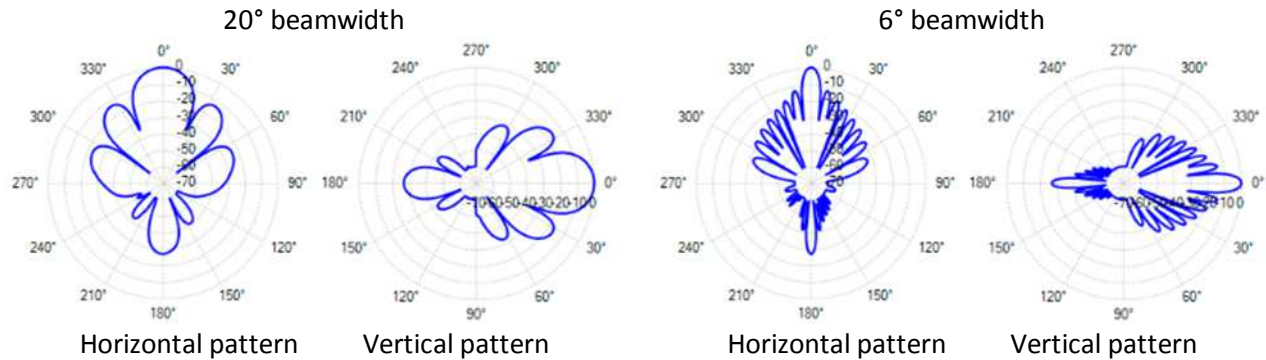


**Figure 14: Antenna radiation patterns for access points in the office scenario**

### 2.5.2 Simulation results

The 500 predicted received powers are plotted in Figure 15 as a function of distance, with LoS and NLoS distinction. The distribution between LoS and NLoS links is illustrated in Figure 16 (left) in function of distance. The longest links between 18 and 21 m are 47% LoS due to the cubicle partitions of low height. The Path Loss Exponent (PLE) is deduced at each frequency and antenna beamwidth. Their values are reported in Figure 17 (right). The LoS PLE is almost constant with frequency. The 6°-beamwidth antenna is acting as a filter that preserves the dominant direct path but remove most indirect paths, thus PLE is almost 2. With larger antenna beamwidth, the canyoning effect (or sum of multiple propagation paths caused by the strong reflections in this confined environment) leads to a received power greater or equal to the LoS direct path power; the observed PLE is decreasing down to 1.8. The NLoS PLE behaves very differently. At lower frequencies, as the transmission losses are weak, the obstructed direct path often remains the dominant path, the NLoS PLE is quite similar to the ones observed in LoS situation. But the multi-path effect becomes dominant at higher frequencies, especially above 28 GHz. As the main component in the received power comes from multiple non-obstructed reflected paths, the PLE is rapidly decreasing, and finally reaches values below 1.5 at 150 GHz. But this decrease in the PLE values is accompanied by a strong increase in the Path Loss Intersect (PLI, i.e. path loss value at distance 1 m) as shown in Figure 17. The average difference between NLoS PLI at 60 GHz and 150 GHz is 16 dB while it is 8 dB in LoS.

The results given in Figure 16 – Figure 18 allows for a simple implementation of an in-office path-loss model in the sub-THz spectrum, where the LoS probability is given as a function of distance, the median path-loss is calculated from frequency-dependent PLE and PLI, and the additional shadowing is considered as a lognormal variable with a frequency-dependent standard-deviation. The graph can be further simplified into approximate formula shown in Table 1, valid in range 90 – 200 GHz.

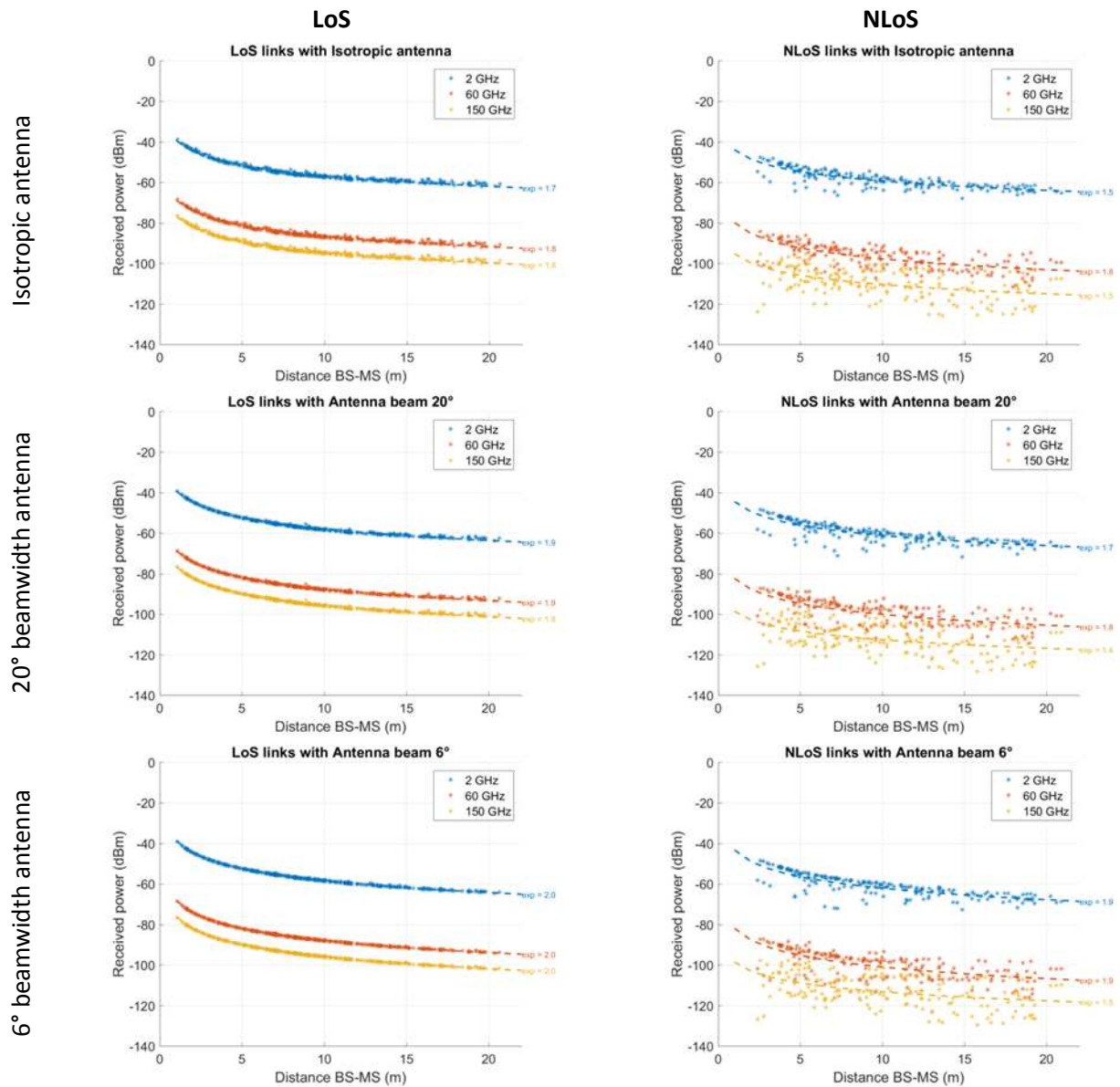


Figure 15: Received power versus distance

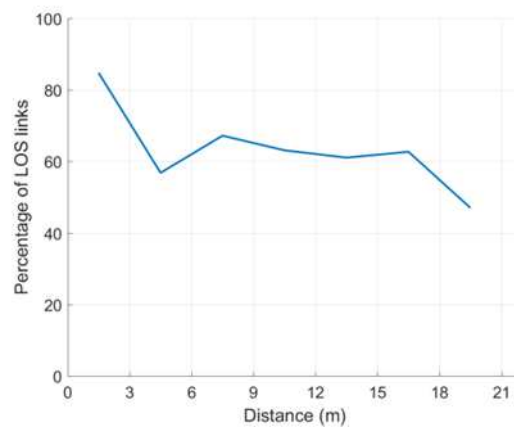


Figure 16: LoS probability vs Distance



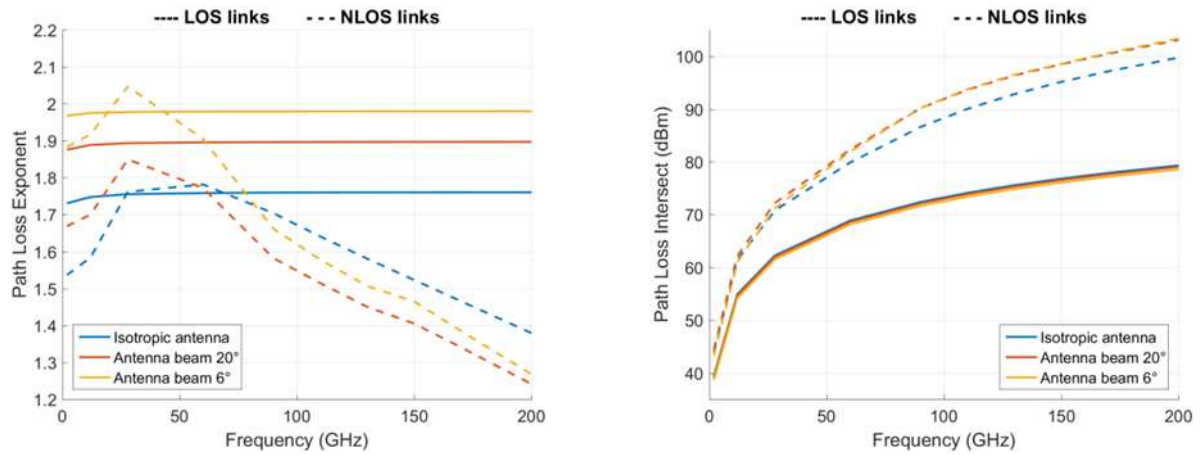


Figure 17: Path loss exponent and Path loss intersect

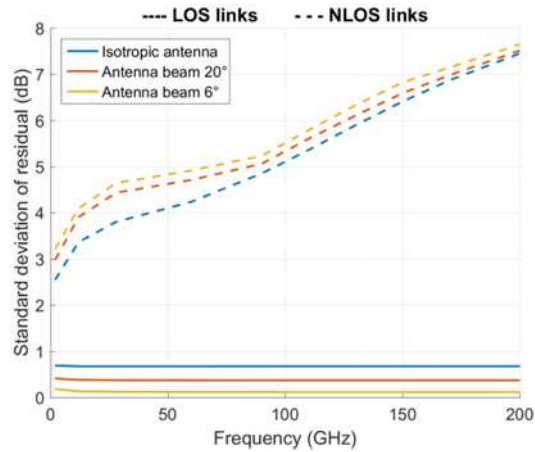


Figure 18: Standard deviation of the shadowing

Table 1: In-office path-loss simplified model

Access point antenna	Isotropic	20°-beamwidth	6°-beamwidth
LoS probability (%)	$77 - 1.3 \times d$		
LoS Path-loss exponent PLE	1.76	1.90	1.98
LoS Path-loss intersect (dB)	$33 + 20 \times \log_{10}(f)$		
LoS shadowing std deviation (dB)	0.7	0.4	0.1
NLoS Path-loss exponent PLE	$1.97 - 0.0029 \times f$	$1.85 - 0.0030 \times f$	$1.97 - 0.0035 \times f$
NLoS Path-loss intersect (dB)	$33 + 28 \times \log_{10}(f)$	$32 + 30 \times \log_{10}(f)$	$30 + 31 \times \log_{10}(f)$
NLoS shadowing std deviation (dB)	$-10 + 3.3 \times \log_{10}(f)$	$-8.9 + 3.1 \times \log_{10}(f)$	$-8.5 + 3.1 \times \log_{10}(f)$

where  $d$  is the distance in meters, and  $f$  is the frequency in GHz.

Those results have been obtained from the prediction of an empty office environment, i.e. without any furniture or people. The presence of additional objects will obviously more strongly impact the propagation at higher frequencies, and therefore will produce higher values for both the PL intersect and PLE in the mmWave and sub-THz spectrum. This is investigated in a second stage of the study, where the 3D office representation is replaced by the one shown in Figure 19. Simulation results are not yet available; they will be reported in next BRAVE deliverable devoted to the physical layer modelling (D2.1).



**Figure 19: Detailed office representation.**

Following, wideband properties of the channel are also computed: horizontal departure angle spreads, horizontal arrival angle spread, delay spread, and coherence bandwidth. They are all computed by considering a maximum range of 30 dB in the wideband received power. They are fully characterized by their Cumulative Distribution Functions (CDF) given in Appendix A. The median values are plotted as a function of the frequency in Figure 20 to Figure 23 with distinction between LoS and NLoS.

The LoS horizontal angle spread at both departure and arrival sides is almost constant with frequency (Figure 20 and Figure 21). When reducing the antenna aperture, it is decreasing very close to  $0^\circ$  as most indirect paths are filtered out. The departure angular diversity is quite similar in NLoS situation, however slightly stronger. The NLoS arrival angle spread is largely increased. The spread tends to reduce with frequency when using directive antenna at the access point. It is below  $10^\circ$  at 150 GHz with  $6^\circ$ -beamwidth aperture. There is no clear trend with an isotropic access point, as the spread remains greater or equal to  $50^\circ$  whatever the frequency is.

The effect of the directive antenna filtering is also observed on the delay spread, which tends to 0 ns with the narrower beam (Figure 22). The LoS delay spread is almost constant with frequency, meaning the major indirect paths remain of same relative magnitude at higher frequencies; they are obviously caused by non-obstructed reflections. The NLoS delay spread versus frequency tends to slowly decrease versus frequency when using a directive antenna, however it is significantly increasing from 2 to 100 GHz with the isotropic access point.

Finally, the coherence bandwidth is larger with the narrowest antenna beams (Figure 23). It is quite constant versus frequency in LoS situation. But the NLoS coherence bandwidth is increasing with

frequency, meaning that the weakest indirect paths are filtered out of the 30 dB power range at the highest frequencies, therefore making the channel more flat.

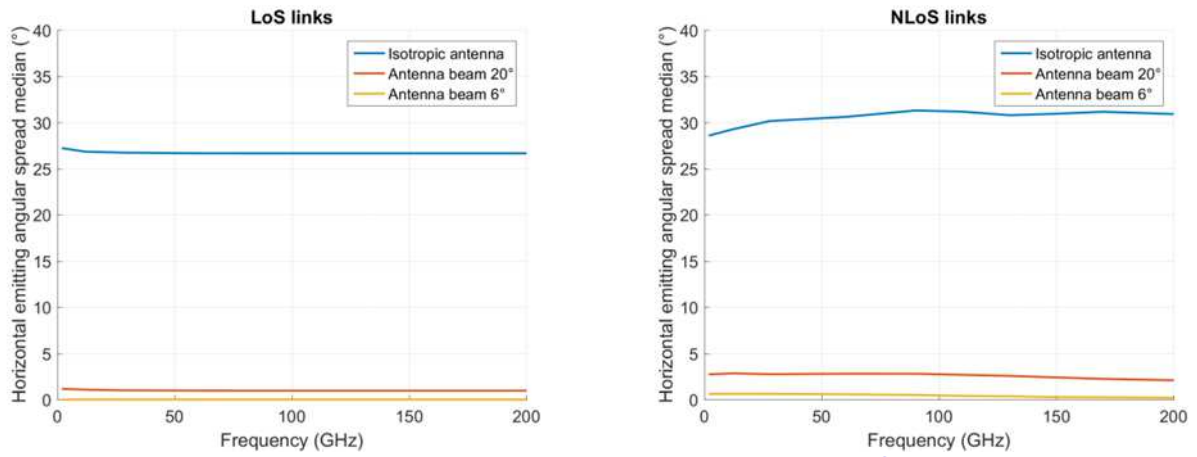


Figure 20: Median horizontal departure angle spread vs frequency.

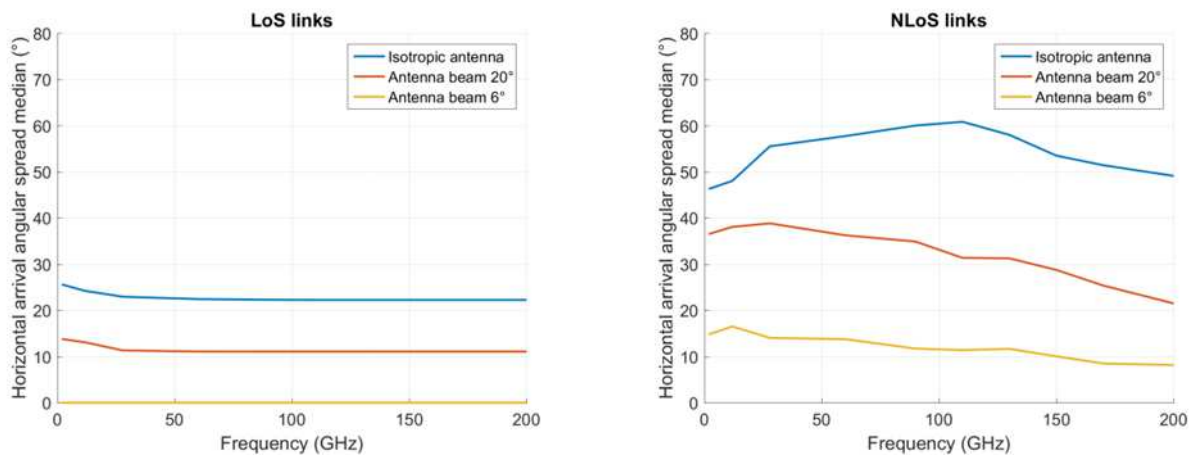


Figure 21: Median horizontal arrival angle spread vs frequency

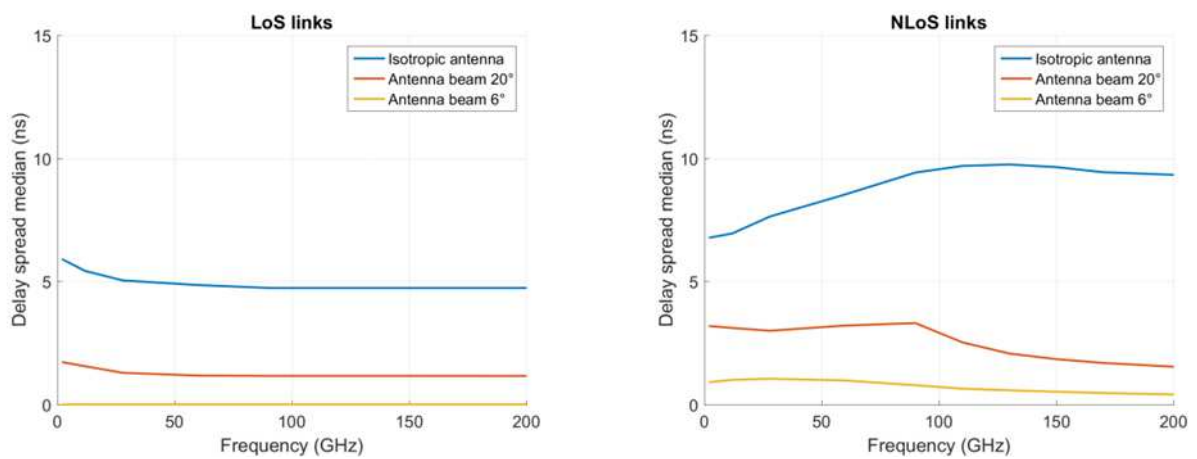


Figure 22: Median delay spread vs frequency

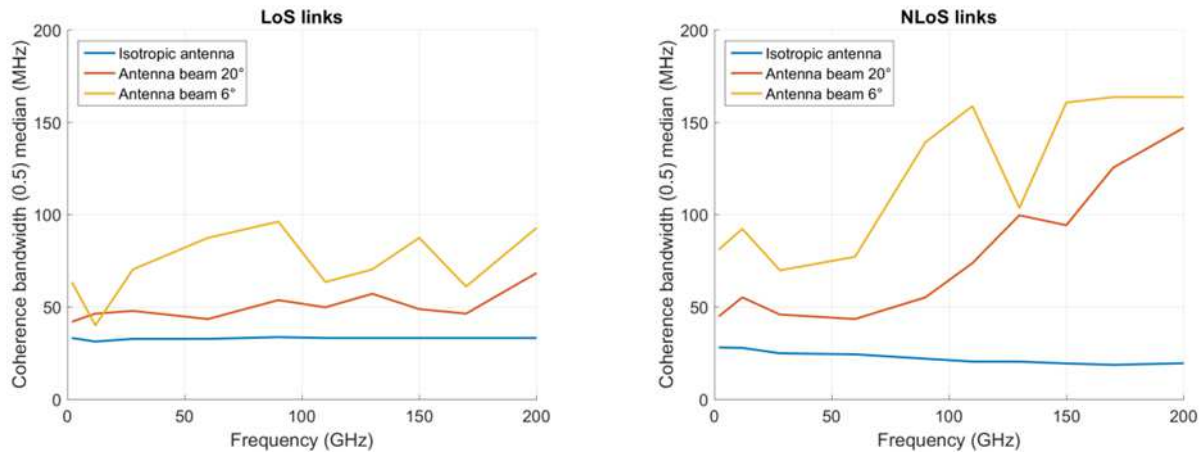


Figure 23: Median coherence bandwidth vs frequency

The power of the propagation paths become naturally weaker at higher frequencies, in the presence of an obstruction or a diffraction. Therefore in a practical channel measurement system, the individual paths are more likely to be received below the noise floor. The wideband characteristics of the measured channel depend both on the maximum allowed power range (*i.e.* difference between power of the strongest path and weakest captured path, *e.g.* 30 dB as considered in our study) and the receiver sensitivity (related to the noise floor). The effect of the receiver sensitivity was not inserted in the previous simulations, however it may produce very different observations on the delay or angle spreads. Figure 24 shows the median delay spread as computed with different receiver sensibilities. The receiver sensibility is supposed to be constant whatever the frequency is (which is very particular situation, but is convenient here for the demonstration).

The conclusion on the delay spread evolution significantly changes depending on the receiver sensitivity value. The NLoS median delay spread is observed as increasing with frequency when the receiver sensitivity is low, while it rapidly falls to only few ns in mmWave or sub-THz frequencies in case of a limited-performance receiver. The way the wideband channel properties are compared at different frequencies has to be done carefully. The delay spread may be strongly reduced in upper spectrum due to the receiver limitations but not directly to the propagation channel.

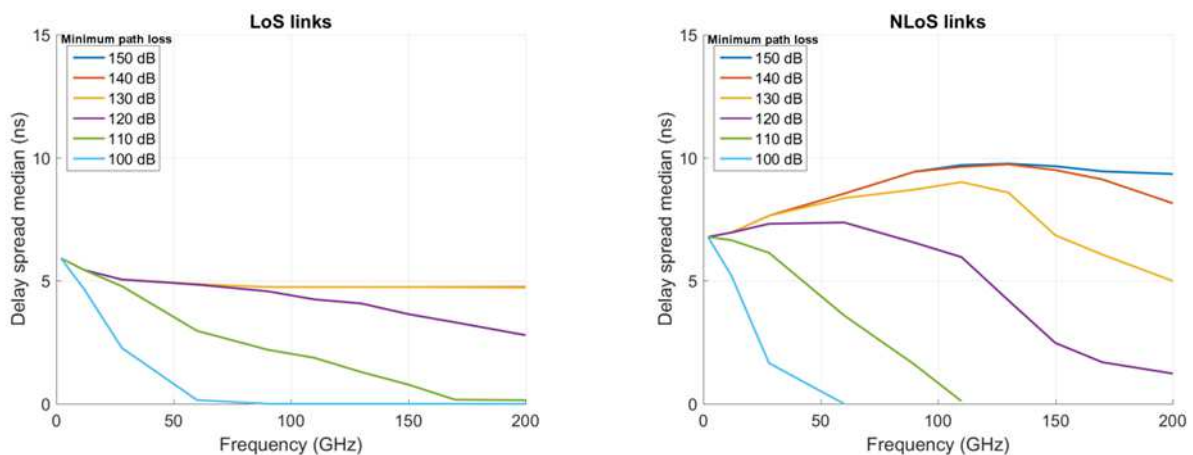


Figure 24: Median delay spread as a function of the minimum path loss



## 2.6 In-street scenario

Prediction and characterization of the outdoor sub-THz propagation channel are conducted for urban fixed backhaul links at street level, typically for antennas installed at lamppost height. LiDAR representation and ray-based multi-paths are together exploited to assess the impact of building and vegetation obstructions.

### 2.6.1 Description

Point cloud LiDAR data that was collected by SIRADEL in the centre of a North-American city (San Jose) is used in this study. The modelled environment is composed of dense buildings with various heights (mostly greater than the simulated antenna heights). Trees are distributed along most of the streets. The study area may be considered as densely vegetated. The street poles, and lampposts in particular, have been precisely classified as shown in Figure 25.



**Figure 25: Urban study area (left) and LiDAR representation (right)**

The lampposts are considered as antenna positions and all lamppost-to-lamppost possible links with range lower than 200 meters are computed at frequency 150 GHz: visibility, multiple paths, and excess path-loss.

Instead of the traditional LoS/NLoS distinction, the links visibility distinguishes between:

- LoS: no obstruction between the two antennas;
- NLoS: building obstruction;
- NLoS-Vegetation: obstruction by only vegetation.

The Excess Path Loss (EPL) is computed for the strongest path, either direct or indirect, assuming that the antennas are highly directive and, therefore, only capture one path. The EPL is given by following formula:

$$EPL = (\text{Predicted path-loss along dominant path}) - (\text{Direct-path Free space loss}) - (\text{Direct-path Gas loss})$$

Where the Direct-path losses are calculated from the direct distance between both antennas.

The environment's impact is better highlighted in the EPL prediction compared to the usual path-loss metric. The propagation channel analysis is thus facilitated.

Two major contributions in this environment are the foliage transmission and foliage masking (computed from diffraction). Transmission may be dominant when the crossed vegetation depth is small or foliage density is low, while diffraction becomes the strongest component when the transmitted path is blocked. Several vegetation linear losses are considered, and compared, in our simulation study: 6, 9 and 12 dB/m. The reason is that the vegetation losses vary with the kind of tree, and actually has not yet been characterized at sub-THz frequencies. Note that the simulated losses are far lower than the ones given by the ITU-R P.833 extrapolation, in agreement with previous observations made by Siradel at millimetre-wave.

## 2.6.2 Simulation results

The distribution between LoS / NLoS and NLoS-Vegetation is shown in Figure 26 (left) as a function of the distance. At shortest ranges, the poles are mostly in LoS and NLoS-Vegetation situations, then NLoS occurrences rapidly increase, and become the dominant configuration after 85 meters. At this distance, the LoS probability falls below 10 %. The NLoS-Vegetation links are less than 20% at range 200 meters.

The CDF of the EPL is plotted in Figure 26 (right) for the three different values of the vegetation linear loss: 6, 9 and 12 dB/m. The NLoS EPL is about 50 dB higher than non-NLoS. It is hardly impacted by the vegetation linear loss value, as the dominant propagation path is often due to rooftop diffraction, i.e. occurs above trees. The LoS percentage appears as the left CDF value in the plain curves: about 20%. The highest CDF values are associated to the NLoS-Vegetation situation, where the vegetation linear loss has a significant impact. As the foliage transmission is combined with foliage diffraction, the distance between EPL curves decreases when the vegetation linear loss increases, i.e. when diffraction becomes dominant.

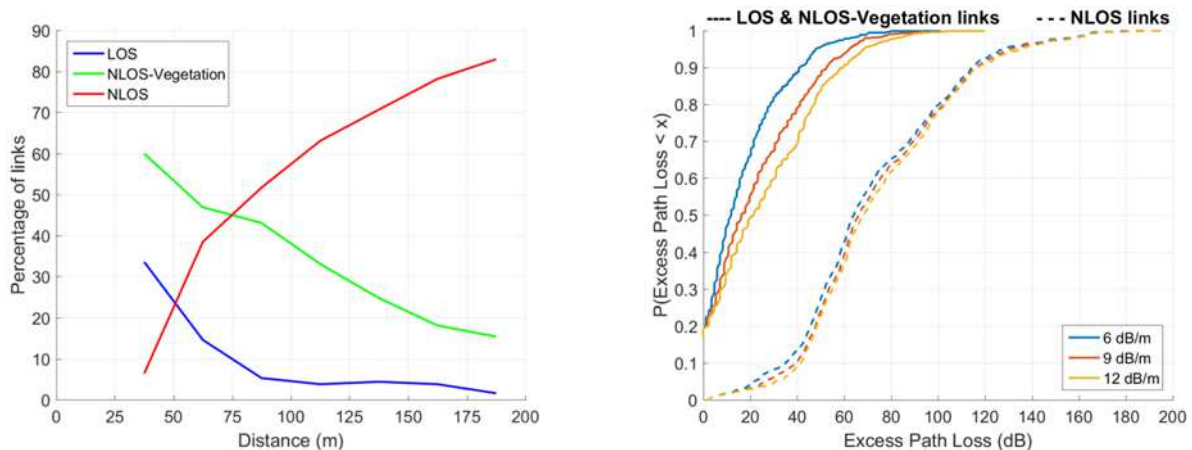


**Figure 26: Distribution of the outdoor propagation results: visibility (left) and Excess Path Loss (right)**

Figure 27 shows all the simulated EPL for NLoS and NLoS-Vegetation links, obtained with the vegetation linear loss of 9 dB/m. The EPL can be approximated by a log-distance dependent function and a lognormal variable with a log-distance dependent standard-deviation:

$$EPL = A + B \times \log_{10}(d) + \mathcal{N}(C(d))$$

Figure 28 shows the resulting EPL fitting functions for the different vegetation linear losses (left), and the standard deviation of the residual path-loss (right). This residual path-loss is very high compared to the

shadowing that is considered at lower frequencies (standard deviation lower or equal to 10 dB). It increases with distance, however the exact trend is obvious.

Finally, the EPL parameters given in Table 2, along with the visibility probabilities shown in Figure 26, are proposed as a simplified model for the path-loss experienced by urban street-level sub-THz fixed backhaul.

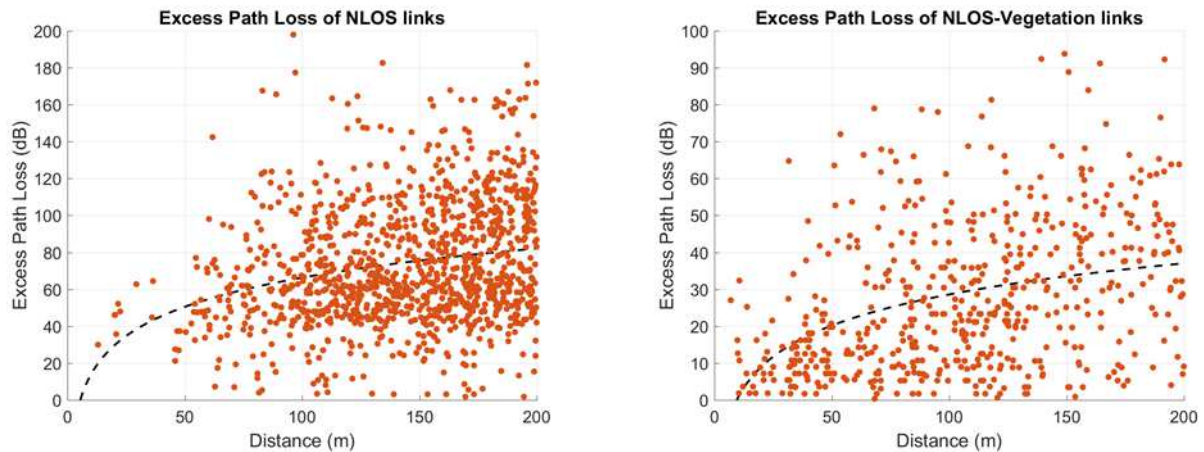


Figure 27: Excess Path Loss of NLoS links (left) and NLoS-Vegetation links (right) for 9 dB/m vegetation linear loss

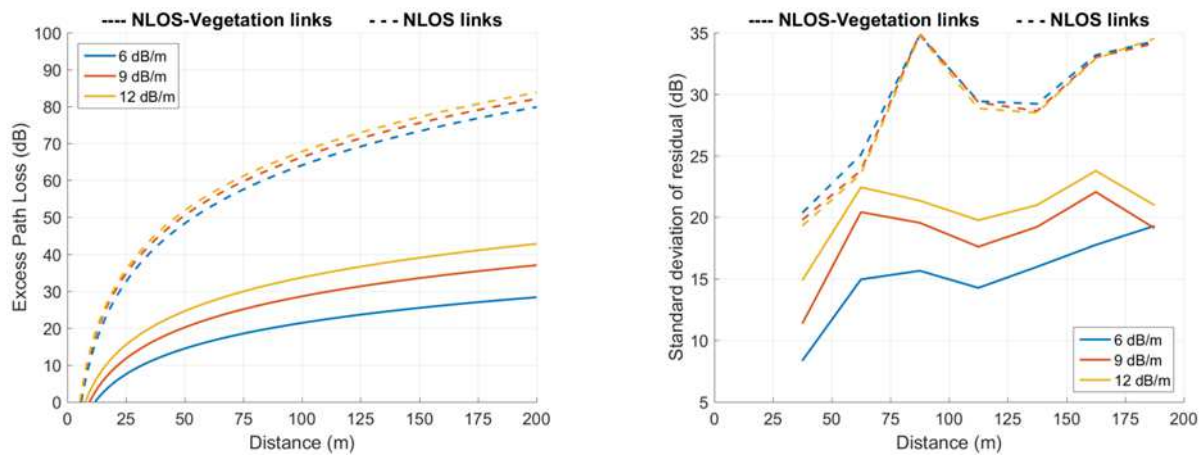


Figure 28: Excess Path Loss fit and standard deviation of the residual

Table 2: Excess path-loss parameters

	A		B		C	
Vegetation linear loss	NLoS-Veg	NLoS	NLoS-Veg	NLoS	NLoS-Veg	NLoS
6 dB/m	-24.8	-40.7	23.1	52.4	$-10.2 + 12.7 \times \log_{10} d$	$-6.1 + 17.8 \times \log_{10} d$
9 dB/m	-27.4	-38.7	28.0	52.5	$-0.9 + 9.7 \times \log_{10} d$	$-8.2 + 18.7 \times \log_{10} d$
12 dB/m	-26.9	-38.6	30.3	53.2	$5.3 + 7.6 \times \log_{10} d$	$-10.1 + 19.5 \times \log_{10} d$

The same simulation model provides coverage maps (received power) as the ones illustrated in Figure 29, assuming 30 dBm of EIRP. The shadow effect behind trees and buildings can clearly be observed; its impact on the connection range is obvious.

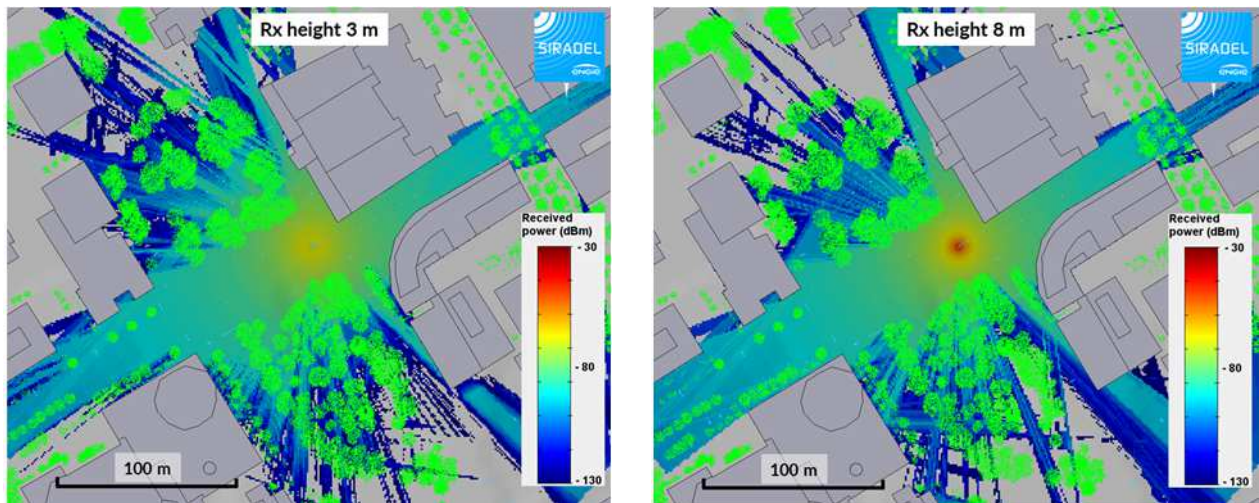


Figure 29: Coverage from a lamppost transmitter towards a 3-meter high receiver (left) and 8-meter high receiver (right)

## 2.7 Perspective

The modelling and implementation work into Volcano prototypes lead to the following current achievements:

- Sub-THz channel simulation for both indoor and outdoor scenarios;
- Application to in-office and outdoor backhaul scenarios for channel characterization;
- Derivation of first and simple path-loss models.

The future perspective into the BRAVE project is three-fold:

1. Extension of the propagation channel characterization. The main research axes are today the introduction of scattering components, the modelling of human body effect, the investigation of scattering phenomena, and the evaluation of the indoor furniture's impact.
2. Exploitation of sub-THz channel samples and/or characteristics into BRAVE techniques design and evaluation.
3. Evaluation and demonstration of promising BRAVE deployment scenarios, including beamforming and massive MIMO communication: performance, constraints, and feasibility.



## 3 RF impairments modelling

### 3.1 Introduction

Radio-Frequency (RF) communications fully rely upon oscillators, an indispensable element of the transmission chain. Their role is to create stable reference signals as to perform two fundamental operations: frequency translation between baseband and passband and In-phase/Quadrature (I/Q) synchronization. As any electronic component, practical RF oscillators present non-ideal characteristics. These hardware imperfections cause random phase noise on the received signal. Along with amplifier non-linearity, I/Q mismatch, phase noise is one of the major RF impairments and may affect severely communication system performance. Nevertheless, decades of research have achieved strong theoretical and practical understanding of noise in oscillators [18-22] and references therein.

With regard to the spectrum shortage in the cellular bands, the sub-THz spectrum 100-300 GHz has aroused lots of interest in the research domain. Considering sub-GHz communications, the phase noise problem is rarely considered. Oscillators at these frequencies demonstrate great reliability such that effects of phase noise may be negligible compared to other RF impairments. In contrast, mmWave systems are critically impacted by phase noise due to the poor performances of high frequency oscillators [23]. The performances of mmWave systems are considerably limited by the oscillator phase noise. In the light of the transistors transient states considerations, the higher the frequency of an oscillator, the worse is its phase noise performance [23].

For a coherent system, the fundamental effect of phase noise is a random rotation of the constellation, which leads to:

- Detection errors resulting in performance degradation;
- Spectral regrowth which may cause user interference;
- In-band signal injection of out-of-band emission;
- Loss of orthogonality for multi-carrier waveforms.

Phase noise has been investigated with the intention to improve oscillators' reliability but also to mitigate its impact on communications. Thereupon, a multitude of phase noise models have been issued and exploited: uniform [24], Gaussian [24], Wiener [18], Tikhonov [18], Leeson's [25], *etc.* Even though, a realistic model of phase noise based on oscillator measurements appears as highly valuable to design robust and efficient systems.

*Contribution:* In this work, we seek to improve the design of robust communication systems affected by phase noise. The first step to achieve this goal is to investigate the generation of phase noise in oscillators. The second step is to study the impact of phase noise in communication systems by evaluating the Shannon capacity for usual phase noise models. With the intention to enhance the analysis of the phase noise impact, we propose a more realistic phase noise model and a versatile simulation architecture directly calibrated upon oscillator spectral measurements.

*Organization:* The remainder of this section is organized as follows. In Section 3.2, a concise description of the phase noise generation mechanism in oscillators is outlined. Further, Section 3.3 discusses how phase

noise impairs communication systems and also presents different phase noise models. Finally, in Section 3.4, a comprehensive phase noise model is proposed along with the corresponding simulation architecture.

## 3.2 Phase Noise in Oscillators

### 3.2.1 Ideal vs noisy oscillators

In communications systems, oscillators are used to perform frequency translation. In the time domain, the complex output  $\hat{v}$  of an ideal oscillator, with normalized amplitude, is expressed as

$$\hat{v}(t) = e^{j 2\pi f_0 t} \quad (3.1)$$

where  $f_0$  is the central frequency of the oscillator. In contrast, when considering a practical oscillator, the output  $v$  is defined by

$$v(t) = [1 + \varepsilon(t)]e^{j(2\pi f_0 t + \phi(t))} \quad (3.2)$$

where  $\varepsilon$  and  $\phi$ , two random independent processes, denote respectively the amplitude noise and the phase noise. Actually, the amplitude noise may be practically eliminated by the application of a limiter on the oscillator output [19]. Therefore and similarly to most of the literature [19] [20] [21] [26], amplitude noise is here considered negligible compared to phase noise.

The most common figure to characterize phase noise performance of an oscillator is its Single SideBand (SSB) spectrum. Namely, the SSB phase noise spectrum  $L(f)$  of an oscillator is obtained throughout the following measurements

$$L(f) = \frac{S_v(f_0 + f)}{P_v} \quad (3.3)$$

with  $S_v$  the Power Spectral Density (PSD) of the oscillator output  $v$ .  $P_v$  is the total power in the signal around the central frequency, which is approximately evaluated by

$$P_v = \int_{\frac{1}{2}f_0}^{\frac{3}{2}f_0} S_v(f) df \quad (3.4)$$

For an ideal oscillator, the whole power would be concentrated at the central frequency  $f_0$  such that  $S_v(f) = \delta(f - f_0)$ , whereas the oscillator phase noise results in spreading the power over frequencies around  $f_0$ . Further, we denote  $S_\phi$  the PSD of phase noise  $\phi$ . The small angle approximation  $e^{j\phi} \simeq 1 + j\phi$  yields for large  $f$

$$S_{\{\phi\}(f)} \simeq L(f) \quad (3.5)$$

Eq. (3.5) draws a direct link between phase noise  $\phi$  and oscillator output  $v$  and enables to calibrate the phase noise model on the oscillator spectral characterizations. Still, close to the central frequency, *i.e.*  $f$  small, this approximation does not hold. Therefore, several researches have been led in order to evaluate and model the near-carrier spectrum of oscillator [21].

### 3.2.2 Noise sources

In the oscillator circuitry, noise sources must be divided into two categories: white and coloured. On the contrary to coloured noise sources, white noise demonstrates a flat spectrum. White noise is the superposition of thermal noise and shot noise. Thermal noise is caused by the Brownian motion of electrons. Shot noise refers to small current fluctuations due to finite charge of an electron and to the randomness of the electron emission.

Meanwhile,  $1/f$  noise presents respectively a PSD with an  $1/f$  characteristic. Also referred to as flicker noise, it is caused by the imperfection of the interface oxide-substrate in transistors. Though there is no proof of  $1/f$  noise stationarity, Stoisiek and Wolf have shown that:

*“The close agreement between theoretical and experimental results demonstrates that the statistical properties of  $1/f$  noise in physical sources are fully consistent with the assumption of stationarity” [27]*

Over the whole circuit, the superposition of all white noise contributions may be represented as a single macro noise source. Similarly,  $1/f$  noise is modelled by a single macro noise source [20]. The distribution of both white and  $1/f$  macro noise sources may be considered Gaussian. From a macroscopic level, this is an illustration of the central limit theorem [28].

### 3.2.3 Phase noise generation mechanism

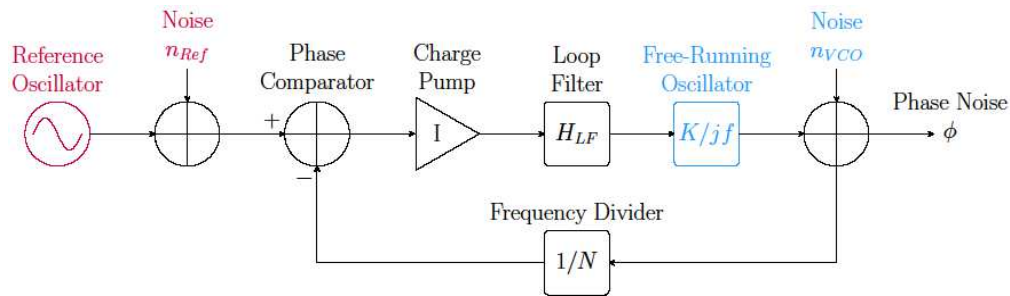


**Figure 30: Simplified LTI model of a PLL stabilized oscillator**

The phase noise generation in oscillators is based on the transformation of amplitude fluctuations  $n$  into phase fluctuations  $\phi$  [21]. In practical systems, a free-running Voltage Controlled Oscillators (VCO) is stabilized to a reference quartz crystal oscillator by means of a Phase-Locked Loop (PLL). A simplified Linear Time Invariant (LTI) model of the oscillator PLL is presented in Fig. 29. One must distinguish the noise introduced by the reference crystal  $n_{Ref}$ , from the free-running oscillator noise  $n_{VCO}$ . From the LTI model of the PLL, we derive the transfer functions  $H_{Ref} = \frac{\phi}{n_{Ref}}$  and  $H_{VCO} = \frac{\phi}{n_{VCO}}$

$$H_{Ref}(f) = \frac{N \cdot I \cdot H_{LF}(f)}{j \cdot 2\pi f \cdot N + I \cdot H_{LF}(f)} \quad (3.6)$$

$$H_{VCO}(f) = \frac{j \cdot 2\pi f \cdot N}{j \cdot 2\pi f \cdot N + I \cdot H_{LF}(f)} \quad (3.7)$$

Given that the PLL is a stable LTI system and that the noise source is a wide-sense stationary process, then the transformation of noise to phase noise may be expressed by

$$S_{\phi}(f) = |H(f)|^2 S_n(f) \quad (3.8)$$

where  $S_{\phi}$  and  $S_n$  are respectively the PSD of phase noise and noise. With regard to the description of the noise sources  $S_n(f) = (K_w + K_c/f)$  and to the PLL LTI model, it can be further derived that

$$S_{\phi}(f) = S_n(f) \cdot \left( \frac{K'}{f^2} + K \right) \quad (3.9)$$

The phase noise generation mechanism is hence the sum of an integration of noise as well as an amplification of it [20] [26] Fig. 30 presents the spectral transformation in oscillators of noise into phase noise, and, in other words, illustrates Eq. (3.9). Fig. 31 is to complete Fig. 30 with the illustration of the resulting phase noise spectrum.

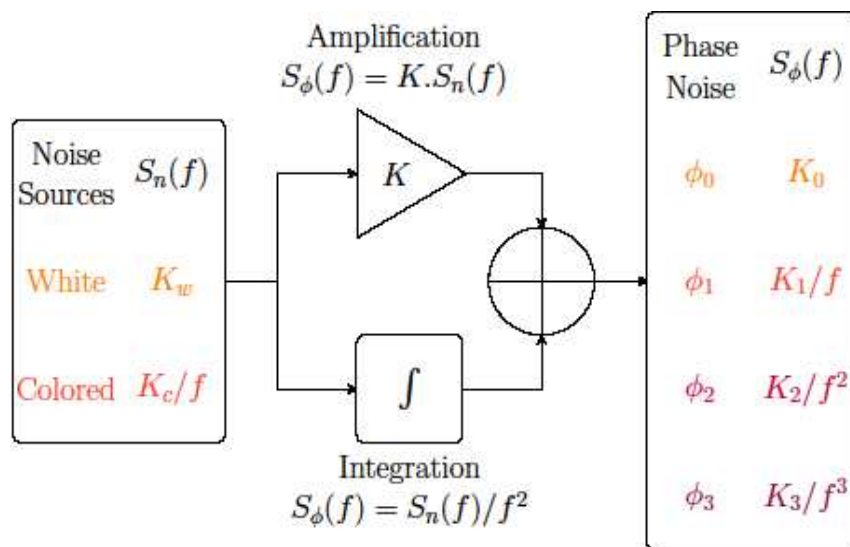


Figure 31: LTI model of the phase noise generation mechanism

### 3.2.4 Phase noise spectrum

Regarding the expressions of the transfer functions  $H_{Ref}$  and  $H_{VCO}$  in Eq. (3.6) and (3.7), it may be pointed out that the PLL behaves as a low-pass filter for the phase noise due to the reference and as a high-pass filter for the free-running oscillator. Thereupon, two distinctive regions may be differentiated in the oscillator spectrum. Below the nominal bandwidth  $\gamma$  of the PLL, the phase noise from the crystal prevails and is referred to as the near-carrier phase noise. While above the cut-off frequency  $\gamma$ , the VCO is the main contribution to phase noise.

With only white noise, an analytical expression for the near-carrier spectrum may be derived, and is a Lorentzian characteristic  $1/(1 + f^2)$ . Though there isn't any exact analytical analysis for white and coloured noise sources, it has been demonstrated in [21] using correlation theory that the Gaussian PSD may be an accurate approximation for near-carrier spectrum.



Far from the central frequency, the spectrum is modelled by a sequence of power law noise as illustrates Fig. 31. It describes the integration of white and coloured noise sources respectively produces  $1/f^2$  and  $1/f^3$  slopes as depicted in Fig. 30. This integration translates the cumulative nature of phase noise. While the amplification of noise sources results in the spectrum as the  $f^0$  and  $1/f$  characteristics.

The recent work in [22] has studied separately the influence of the different spectrum regions on communication systems. Considering pilot based communication, it has been shown that low-frequency phase noise events  $f < \gamma$  does not affect significantly the system performance. This results holds as long as  $\gamma$  is relatively small to the symbol rate  $1/T$ . Furthermore, it has been found that the influence of the different regions strongly depends on the communication bandwidth  $1/T$ . In particular, more than the other spectrum regions, the noise floor  $f^0$  has the strongest impact on systems with high symbol rate. This may be intuitively explained by the observation that the phase noise bandwidth  $K_1/K_0$  is a small contribution to the overall phase noise impeding the system. On the contrary, low symbol rate systems are more sensitive to noise regions with  $1/f^\alpha$  slopes. In this case, the phase noise bandwidth represents a larger contribution with regard to the system bandwidth.

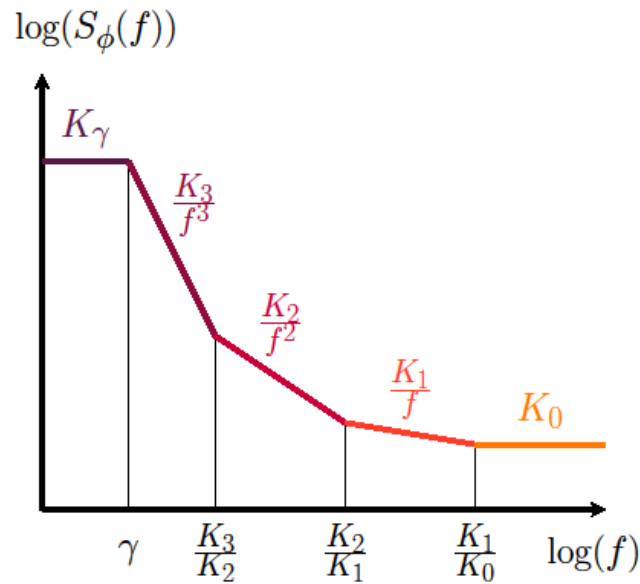


Figure 32: Phase noise spectrum

### 3.3 Impact of Phase Noise in Communication Systems

#### 3.3.1 Communication system model

Considering a single carrier communication system, the transmitted signal  $x$  is expressed as

$$x(t) = \sum_{n=1}^N s[n]p(t - nT) \quad (3.10)$$

where  $s$  is the modulated symbol from the complex constellation  $C$ ,  $n$  is the transmitted symbol index,  $T$  is the symbol duration, and  $p$  is the band-limited square-root Nyquist shaping pulse function with unit-

energy. Then, the continuous time complex baseband received signal, affected by the oscillator phase noise  $\phi$ , may be written as

$$r(t) = x(t)e^{j\phi(t)} + \hat{w}(t) \quad (3.11)$$

with  $\hat{w} \sim CN(0, \sigma_{\hat{w}}^2 = N_0)$  representing a circularly symmetric complex Additive White Gaussian Noise (AWGN) with spectral density  $N_0$ . The received signal  $y$  is passed through a matched filter :  $t \rightarrow p^*(-t)$  such that

$$y(t) = \int_{-\infty}^{+\infty} \sum_{n=1}^N s[n]p(t - nT - \tau)p^*(-\tau)e^{-j\phi(t-\tau)}d\tau + \int_{-\infty}^{+\infty} \sum_{n=1}^N \hat{w}(t - \tau)p^*(-\tau)d\tau \quad (3.12)$$

Variations of phase noise may be considered small over a symbol duration if the phase noise bandwidth  $B_{pn} = K_0/K_1$  is small compared to system bandwidth  $B = 1/T$

$$B_{pn} \ll B \quad (3.13)$$

The slow-varying phase noise hypothesis is assumed in most of the literature [20] [22]. Nonetheless, a couple of papers [29] [30] pursues the analysis considering fast-varying phase noise. In particular, oversampling might be beneficial in case of fast-varying phase noise [30].

Here, it is assumed that the phase noise is constant over a symbol duration  $T$  and that the channel gain is perfectly mitigated. Then, by sampling the matched filter output at  $nT$  times instances, the received symbol is defined with the discrete time notation by

$$y[n] = s[n]e^{j\phi[n]} + \omega[n] \quad (3.14)$$

where  $\omega \sim CN(0, \sigma_n^2 = N_0/T)$  is the band-limited AWGN.

### 3.3.2 Capacity of the phase noise channel

The impact of phase noise on a communication system may be evaluated by deriving the Shannon capacity. In order to compare systems affected by phase noise to reference systems, the channel capacity appears as a valuable tool. Lapidot derived a fundamental result for channel capacity in presence of phase noise at high SNR in [31]. Considering a not uniformly distributed phase noise with memory, the capacity is expressed by

$$C = \frac{1}{2} \log_2 \left( 1 + \frac{SNR}{2} \right) + \log_2(2\pi) - h(\{\phi\}) + o(1) \quad (3.15)$$

where  $SNR = \sigma_x^2 / \sigma_n^2$  and  $h(\phi)$  is the differential entropy rate of the phase noise defined by

$$h(\{\phi\}) = \lim_{n \rightarrow \infty} h(\phi[1], \phi[2], \dots, \phi[n]) \quad (3.16)$$

In the case of memoryless phase noise, we have  $h(\{\phi\}) = h(\phi)$  the differential entropy of the phase noise.

#### 3.3.2.1 Non-coherent systems

Non-coherent systems may simply be modelled with a uniformly distributed phase noise over  $[0, 2\pi)$  such that

$$\phi \sim U(0, 2\pi) \quad (3.17)$$

$$h(\phi) = \log_2(2\pi) \quad (3.18)$$

Subsequently, the capacity of a non-coherent system is given by

$$C = \frac{1}{2} \log_2\left(1 + \frac{SNR}{2}\right) + o(1) \quad (3.19)$$

As expected, the phase noise has no impact on the capacity as information is carried by amplitude.

### 3.3.2.2 Partially coherent systems

When a system employs a PLL at their receiver as a phase tracker to lock on the received carrier, it may be referred to as partially coherent. The output signal of a PLL subject to white noise presents residual phase errors described by a Wiener process. And under the assumption of high Signal-to-Noise Ratio, the steady state of phase errors may be described as a stationary memoryless process following a Tikhonov distribution [18]

$$f_\phi = \frac{e^{\lambda \cos \phi}}{2\pi I_0(\lambda)} \quad (3.20)$$

where  $\lambda$  is the SNR and  $I_0$  is the 0-order modified Bessel function. A Tikhonov distribution (also known as von Mises distribution) may be closely approximated by a wrapped Gaussian. The Tikhonov distribution maximizes the entropy for a given phase noise variance with

$$h(\phi) = \log_2(2\pi I_0(\lambda)) - \lambda \frac{I_0(\lambda)}{I_1(\lambda)} \quad (3.21)$$

For  $\lambda = 0$ , the Tikhonov distribution becomes the circular uniform distribution and the entropy attains its maximum value of  $\log_2(2\pi)$ .

### 3.3.2.3 Gaussian model

Gaussian model is exploited for mathematical convenience in order to derive a simple analytical analysis. For phase noise modelled as a Gaussian process [24]

$$\phi \sim N(0, \sigma_{pn}^2) \quad (3.22)$$

The Gaussian distribution is a relevant phase noise model when considering wide bandwidth systems in which the oscillator noise floor is the greatest contributor [22]. The differential entropy of a normally distributed variable  $\phi \sim N(0, \sigma_{pn}^2)$  is a well-known result and is given by

$$h(\phi) = \frac{1}{2} \log_2(2\pi e \sigma_{pn}^2) \quad (3.23)$$

### 3.3.2.4 Wiener process

Wiener process is an extensively used phase noise model in the literature. It relates to the integration of white noise by the oscillator. The phase noise describes a random cumulative process which is defined as a Gaussian random walk

$$\phi[n] = \phi[n-1] + \Delta[n] \quad (3.24)$$

with  $\Delta \sim N(0, \sigma_\Delta^2)$ . As shown in [26], if the noise is defined by a Wiener process, then its differential entropy rate may be approximated by

$$h(\{\phi\}) \simeq \frac{1}{2} \log_2(2\pi e \sigma_\Delta^2) \quad (3.25)$$

#### 3.3.2.5 Leeson's model

Leeson's model is the historical reference [25] and certainly the most used model. The oscillator phase noise is defined by the superposition of three random processes

$$\phi[n] = \phi_3[n] + \phi_2[n] + \phi_0[n] \quad (3.26)$$

where  $\phi_0$  represents a white noise source, while  $\phi_3$  and  $\phi_2$  present cumulative natures

$$\phi_3[n] = \phi_3[n-1] + \Delta_3[n] \quad (3.27)$$

$$\phi_2[n] = \phi_2[n-1] + \Delta_2[n] \quad (3.28)$$

here, the phase increments  $\Delta_2$  and  $\Delta_3$  relate respectively to the integration of white and  $1/f$  noise sources in the PLL. Eventually, the Leeson's model describes the following spectrum

$$S_\phi(f) = \sum_{\alpha} \frac{K_{\alpha}}{f^{\alpha}}, \text{ with } \alpha \in \{0, 2, 3\} \quad (3.29)$$

It may be observed here that latter equation does not model does a  $1/f$  characteristic. In practice, this characteristic demonstrates a spectral density below the  $1/f^2$  and  $1/f^0$  ones. It is therefore not modelled in the Leeson's phase noise spectrum.

### 3.4 Realistic Phase Noise model and Simulation

#### 3.4.1 Proposed model

The proposed model is directly related to the phase noise generation mechanism previously described in Fig. 30. Two regions of the spectrum are being differentiated with regard to section 3.2. Subsequently, the phase noise may be expressed as

$$\phi[n] = \phi_{VCO}[n] + \phi_{Ref}[n] \quad (3.30)$$

Such that, below the PLL bandwidth  $\gamma$ , the phase noise from reference crystal  $\phi_{Ref}$  prevails and is modelled as flat. Above  $\gamma$ , the phase noise from the free running oscillator prevails and describes a sequence of power law characteristics  $1/f^3, 1/f^2, 1/f^1, f^0$ . The phase noise from the free running oscillator is the sum of four contributions and may be described by

$$\phi_{VCO}[n] = \phi_3[n] + \phi_2[n] + \phi_1[n] + \phi_0[n] \quad (3.31)$$

where  $\phi_0$  and  $\phi_1$  describes a white and a  $1/f$  noise sources. While  $\phi_3$  and  $\phi_2$  are defined by

$$\phi_3[n] = \phi_3[n-1] + \Delta_3[n] \quad (3.32)$$

$$\phi_2[n] = \phi_2[n-1] + \Delta_2[n] \quad (3.33)$$

Similarly to the Leeson's model, the phase increments  $\Delta_i$  relate to the integration of white and colored noise sources. The PSD of the phase noise model is similar to the one illustrated in Fig. 31, and can be written as

$$S_\phi(f) = \frac{K_\gamma}{1 + \frac{f}{\gamma^4}} + \sum_{\alpha} \frac{K_\alpha}{f^\alpha} + \gamma^\alpha, \quad \text{with } \alpha \in \{0,1,2,3\} \quad (3.34)$$

where constant  $K_\alpha$  correspond to the spectral characteristic  $K_\alpha/f^\alpha$  measured on the oscillator.

### 3.4.2 Simulation

#### 3.4.2.1 Two regions spectrum

In this section, an architecture to simulate phase noise related to the proposed model is outlined. Fig. 3.4 illustrates this architecture. The generated phase noise presents same PSD as in Fig. 31. The phase noise  $\phi_{Ref}$  from the reference crystal is generated by low pass filtering zero-mean Gaussian random samples  $w_\gamma$  with variance  $\sigma_\gamma^2 = K_\gamma$ . Phase noise from the free running oscillator  $\phi_{VCO}$  is generated by high-pass filtering the four different random processes  $\phi_\alpha$ ,  $\alpha \in \{0,1,2,3\}$ . The low-pass and high-pass filters are implemented by means of Chebyshev filters of type II. Respectively,  $\phi_\alpha$  represents a phase noise with a PSD characteristic of  $1/f^\alpha$  and is generated from the filtering of Gaussian samples as described in the following paragraph.

#### 3.4.2.2 Discrete simulation of power law noise

In [32], Kasdin proposed a two steps method to generate random samples which present a power spectral density of  $1/f^\alpha$ :

- i. Generate random Independent Identically Distributed (IID) samples with a Gaussian distribution  $N(0, \sigma_\alpha^2)$ .
- ii. Pass these samples through a linear filter with an impulse response  $H_\alpha$  described by

$$H_\alpha(z) = (1 - z^{-1})^{-\frac{\alpha}{2}} \quad (3.35)$$

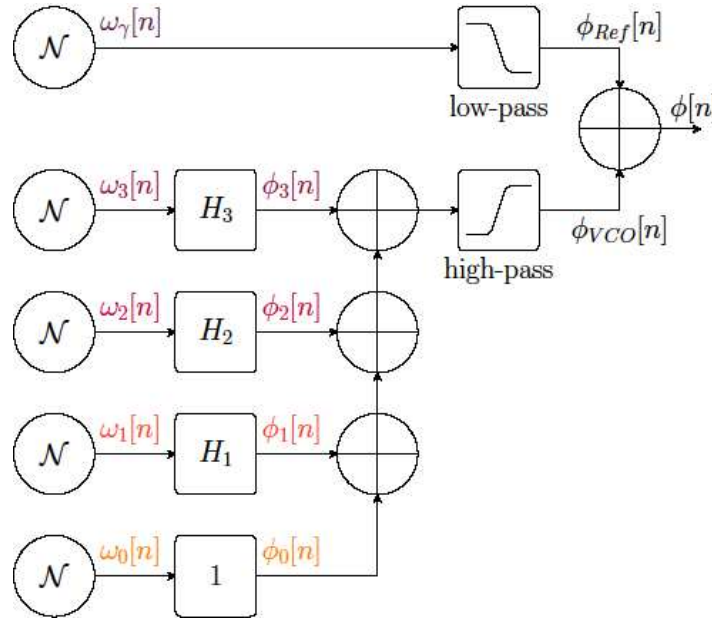


**Figure 3.4: Realistic phase noise generator**

The simulated noise presents a PSD defined by

$$S_{\phi_\alpha}(f) = \sigma_\alpha^2 \cdot T \cdot H_\alpha(z) \cdot H_\alpha(z^{-1}) \quad (3.36)$$

With  $z = e^{j2\pi fT}$ . After applying Euler's formula

$$S_{\phi_\alpha}(f) = \sigma_\alpha^2 \cdot \frac{T}{(2\sin(\pi fT))^\alpha} \quad (3.37)$$

Further, when the phase noise bandwidth is small compared to the system one, *i.e.*  $fT \ll 1$

$$S_{\phi_\alpha}(f) \simeq \frac{\sigma_\alpha^2 T}{(2\pi fT)^\alpha} \quad (3.38)$$

Eventually, if the variance of Gaussian random samples is set to verify  $\sigma_\alpha^2 = (2\pi)^\alpha K_\alpha T^{\alpha-1}$ , where  $K_\alpha$  is obtained from spectral measurements on oscillator, then one obtain the desired spectral characteristic

$$S_{\phi_\alpha}(f) = \frac{K_\alpha}{f^\alpha} \quad (3.39)$$

#### 3.4.2.3 Implementation of filter $H_\alpha$

The filtering process is realized in the time domain by a convolution with the discrete impulse response  $h = [h_0, h_1, \dots, h_N]$ . The coefficients  $h_k$  may be expressed from the power series expansion of the transfer function

$$H_\alpha(z) = (1 - z^{-1})^{\frac{\alpha}{2}} \quad (3.40)$$

$$H_\alpha(z) = 1 + \frac{\alpha}{2} z^{-1} + \frac{\alpha}{2} \cdot \left(1 + \frac{\alpha}{2}\right) z^{-2} + \dots \quad (3.41)$$

Such that  $h_k$  is the  $k$ -th derivative of  $(1 - z^{-1})^{-\frac{\alpha}{2}}$  evaluated at  $z = 0$ .

These coefficients present a recursive relation

$$h_0 = 1$$

$$h_k = h_{k-1} \cdot \frac{k - 1 + \frac{\alpha}{2}}{k} \quad (3.42)$$

The number of coefficients  $N$ , *i.e.* the length of the impulse response, is to be set under a complexity and accuracy trade-off.

#### 3.4.2.4 Generalized model

Empirical observations have shown the existence of a  $1/f^4$  characteristic in the oscillator phase noise spectrum [31][32] This  $1/f^4$  PSD may be referred to as the random walk frequency and is related to the oscillator environment such as temperature variations, mechanical vibrations, etc.

In order to achieve a flexible phase noise model that match more accurately the spectral characterizations of the oscillator, let us release the constraint of integer power law phase noise by generalizing our model to

$$S_\phi(f) = \frac{K_\gamma}{1 + \left(\frac{f}{\gamma}\right)^8} + \sum_{\alpha} \frac{K_\alpha}{f^\alpha + \gamma^\alpha}, \quad \text{with } \alpha \in \{\alpha_i\} \quad (3.43)$$

Here  $\{\alpha_i\}$  may represent any measured slope, *e.g.*  $\{\alpha_i\} = \{0.2, 1.6, 3.2\}$  with the corresponding  $K_\alpha$  measured values. The simulator described in Fig. 3.4 still holds perfectly and may be used with real values of  $\alpha$ .

### 3.5 Conclusion and future work

In this work, we intend to provide analytical tools for sub-THz communication design and circuit specification. A model is, by definition, a trade-off between accuracy and complexity of description. In contrast to most of the literature, we privilege the low complexity of a model rather than its accuracy. In practice, performant scheme design relies on analytical analyses. As future work we propose to discuss the appropriate choice of phase noise model with regard to oscillator spectral characterizations. The Gaussian distribution will be confronted to the conventional but more complex Wiener model as well as state-of-the-art oscillator (plus PLL) components designed for sub THz applications.

In order to demonstrate how the mathematical convenience of the Gaussian model could be exploited to optimize constellations and improve demodulation performance in the presence of PN, we propose, in the next section to derive an optimized demodulator for M-QAM modulations when signal is corrupted by phase noise. The optimal signal processing as well as some performance assessments are given.

## 4 Application: Optimum Demodulation in the Presence of Gaussian Phase Noise

### 4.1 Introduction

The poor performance of high frequency oscillators [33] plagues sub-THz systems with strong Phase Noise (PN). This has motivated extensive work on the design of optimum receivers for systems impacted by PN. Numerous of these optimum receivers are listed in [34] for the common PN models. Still, most of the literature's detectors present complex structures hindering any analytical study. The development of telecommunications has proved that simple analytical frameworks are fundamental for the design of communications systems as they provide means to pursue comprehensive analyses and thus develop efficient algorithms.

Through this work, we aim at improving the design of high-rate sub-THz communications. It mainly pursues the study of Krishnan [34]. Similarly, we assume a high SNR and a Gaussian PN to derive the already known Maximum-Likelihood (ML) decision premetric for symbol detection. In contrast to [34], we exploit further the high SNR approximation to properly define the *polar metric*. Our metric achieves the same optimum performance of the *ML premetric* but enables us to come within the scope of complete metric spaces. Representing signals upon an appropriate metric space allows the use of efficient algorithms to perform the demodulation. Further, to enhance performance of coded systems, we propose computable probabilistic demapper values using the polar metric to implement efficient soft decision decoding. Though knowledge of the channel statistics improves the performance, it requires a channel estimation. Accordingly, we propose ML estimators of the thermal and phase noise variances. The performance degradation due to estimation errors of the polar metric are eventually evaluated and compared to the ML premetric one.

The remainder of this chapter is organized as follows. Section 4.2 introduces a brief description of the channel and PN models. Section 4.3 derives the polar metric decision rule for optimal symbol detection impacted by Gaussian PN. Further, Section 4.4 is devoted to the evaluation of probabilistic demapper values. Finally, an appropriate channel estimation is proposed in Section 4.5 to implement the optimal demodulation.

### 4.2 System Model

#### 4.2.1 Channel

We consider the complex Additive White Gaussian Noise (AWGN) channel impacted by PN. The received signal is then written as

$$r = s \cdot e^{j\phi} + n, \quad (4.1)$$

where  $s$  is the modulated symbol,  $\phi$  is the oscillator PN and  $n$  represents a zero-mean circular complex Gaussian noise with variance  $2\sigma_n^2$ . The transmitted symbol  $s$  belongs to the constellation  $\mathcal{C}$  with average energy  $E_s$  and modulation order  $M$ . We will use the polar representation such that  $s_\rho$  and  $s_\theta$  stand respectively for the amplitude and phase of symbol  $s$ .



### 4.2.2 Phase noise

As mentioned in the previous chapter, the Gaussian appears to be an appropriate PN model for sub-THz systems. Indeed, when considering wide bandwidth systems, the oscillator noise floor represents the greatest contribution to the overall PN [35]. Then the oscillator PN  $\phi$  is to be described by a zero-mean Gaussian distribution with variance  $\sigma_p^2$  as follows

$$\phi \sim N(0, \sigma_p^2). \quad (4.2)$$

## 4.3 Maximum Likelihood Symbol Detection

### 4.3.1 Optimum decision metric at high SNR

Regarding symbol-by-symbol detection, the Symbol Error Probability (SEP) is minimized by the Maximum *A Posteriori* (MAP) decision criterion [36]. When transmitted symbols are equiprobable and mutually independent, this criterion simplifies to the ML decision rule [36]. The optimum receiver decision is hence defined upon the likelihood function  $p(r|s)$ . With regard to the channel model in Eq. (4.1) it is relevant to rewrite

$$p(r|s) = p(r_\rho, r_\theta | s_\rho, s_\theta). \quad (4.3)$$

Let us denote by  $n'$  the shifted noise  $n \cdot e^{-j(s_\theta + \phi)}$  which is identically distributed to  $n$  as the complex AWGN is circular. We then study the received symbol through its amplitude and phase as

$$\begin{aligned} r_\rho &= |s_\rho + n'| \cdot e^{j(s_\theta + \phi)} \quad (4.4) \\ &= \sqrt{(s_\rho + \Re(n'))^2 + \Im(n')^2} \\ &\simeq s_\rho + \Re(n') \end{aligned}$$

and

$$\begin{aligned} r_\theta &= \arg[(s_\rho + n') \cdot e^{j(s_\theta + \phi)}] \quad (4.5) \\ &= s_\theta + \phi + \arctan\left(\frac{\Im(n')}{s_\rho + \Re(n')}\right) \\ &\simeq s_\theta + \phi + \frac{\Im(n')}{s_\rho}. \end{aligned}$$

These first-order approximations clearly hold under a high SNR assumption. Further, exploiting the high SNR assumption enables to derive a simple closed-form expression of the channel likelihood function [34]. We conclude from the thermal and phase noise model in Eq. (4.1) and (2) that

$$r_\rho \sim N(s_\rho, \sigma_n^2), \quad (4.6)$$

$$r_\theta \sim N\left(s_\theta, \sigma_p^2 + \frac{\sigma_n^2}{s_\rho^2}\right).$$

It is straightforward that the likelihood function follows a bivariate Gaussian distribution defined by

$$p(r|s) = \frac{\exp\left(-\frac{1}{2}\left(\frac{(r_\rho - s_\rho)^2}{\sigma_n^2} + \frac{(r_\theta - s_\theta)^2}{\sigma_p^2 + \frac{\sigma_n^2}{s_p^2}}\right)\right)}{2\pi \sqrt{\sigma_n^2\left(\sigma_p^2 + \frac{\sigma_n^2}{s_p^2}\right)}}. \quad (4.7)$$

This expression has been originally derived in [34] and leads to the ML detection decision at the receiver given by

$$\begin{aligned} \hat{s} &= \arg \max p(r|s), \quad s \in \mathcal{C} \quad (4.8) \\ &= \arg \min d^2(r, s), \end{aligned}$$

where  $d$  is the *ML premetric* defined by

$$d^2(r, s) = \frac{(r_\rho - s_\rho)^2}{\sigma_n^2} + \frac{(r_\theta - s_\theta)^2}{\sigma_p^2 + \frac{\sigma_n^2}{s_p^2}} + \log\left(1 + \frac{1}{\sigma_p^2} \cdot \frac{\sigma_n^2}{s_p^2}\right). \quad (4.9)$$

The ML premetric has proved to yield significant gain in performance compared to the Euclidean distance detector [34]. This decision rule is the minimization of the Mahalanobis distance [37]. However, in this case the covariance matrix is defined upon the amplitude of the sent symbol  $s_p$ . Therefore, considering  $d$  is not convenient since it does not define a metric. Indeed, the map  $d: \mathcal{C} \times \mathcal{C} \mapsto \mathbb{R}^+$  is neither symmetric nor subadditive - even if the  $\log$  term is considered negligible in the decision.

Without loss of generality, we can assume that  $\sigma_p^2 + \frac{\sigma_n^2}{s_p^2} \simeq \sigma_p^2 + \frac{\sigma_n^2}{E_s}$ , which is a tight approximation in a high SNR and strong PN scenario. This leads to the *polar metric* decision rule

$$\hat{s} = \arg \min d_\gamma^2(r, s), \quad s \in \mathcal{C} \quad (4.10)$$

$$d_\gamma^2(r, s) = (r_\rho - s_\rho)^2 + \frac{(r_\theta - s_\theta)^2}{\gamma^2},$$

where  $\gamma^2 = \frac{\sigma_p^2}{\sigma_n^2} + \frac{1}{E_s}$ . One of the advantages of exploiting the polar metric rather than the ML premetric is that distances are simpler to evaluate on practical systems. Besides, in doing so, the polar metric  $d_\gamma$  is well-defined and enables us to pursue the analysis within the scope of complete metric space.

### 4.3.2 Framework

**Lemma 4.1 :** Let the complex number  $s$  be represented by its polar coordinates  $(s_\rho, s_\theta) \in P = [0, \infty) \times [-\pi, \pi]$ . Then the space  $P^N$  - of sequences  $\mathbf{s} = \{s_{\rho,k}, s_{\theta,k}\}_{1 \leq k \leq N}$  of  $N$  numbers in  $P$  - is a complete metric space when equipped with the metric  $d_\gamma: P^N \times P^N \mapsto R^+$  defined by

$$d_\gamma^2(\mathbf{x}, \mathbf{y}) = \sum_{k=1}^N (x_{\rho,k} - y_{\rho,k})^2 + \frac{(x_{\theta,k} - y_{\theta,k})^2}{\gamma^2}, \quad \gamma^2 \in R_+^* \quad (4.11)$$

for every  $\mathbf{x}, \mathbf{y}$  vectors of  $P^N$ .

*Proof:* It is sufficient to demonstrate that  $P^N$  is a closed subset of the complete metric space  $(R^{2N}, d_\gamma)$ . First, it is trivial that the map  $d_\gamma$  is a weighted Euclidean distance on  $R^{2N}$ . It follows immediately that  $(R^{2N}, d_\gamma)$  is a complete metric space. Ultimately, the metric space  $(P^N, d_\gamma)$  is complete as  $P^N$  is clearly a closed subset of  $R^{2N}$ .

From now on, we will abbreviate by  $p_2$  the metric space  $(P^N, d_\gamma)$  providing the framework to study the Gaussian PN channel. Metric spaces, by generalizing the notion of distances, provide a fundamental framework for telecommunications. Lemma 4.1 ensures that efficient algorithms may be designed for the demodulation of signals over the Gaussian PN channel. By way of example, the Nearest Neighbor (NN) search to realize the symbol detection or to compute the probabilistic demapper values - later defined - may be performed very efficiently within  $p_2$  using projections or sphere decoding. However, design of such algorithm exceeds the scope of this paper and is to be addressed in a future dedicated one.

To conclude, it is important to highlight the strong similarity of the Gaussian PN channel and the complex AWGN one. This is well illustrated by the fact that the system model in Eq. (4.1) and (4.2) can be approximated within  $P$  by

$$(r_\rho, r_\theta) \simeq (s_\rho + n_\rho, s_\theta + n_\theta), \quad (4.12)$$

where  $n_\rho$  and  $n_\theta$  follow Gaussian distributions with respect to (4.6). In fact, we entitled the space  $p_2$  by analogy to the space  $l_2$  - the set of complex-valued sequences equipped with the Euclidean inner product - usually exploited to study discrete signals over linear channels.

### 4.3.3 Application: demodulation of uncoded $M$ -QAM

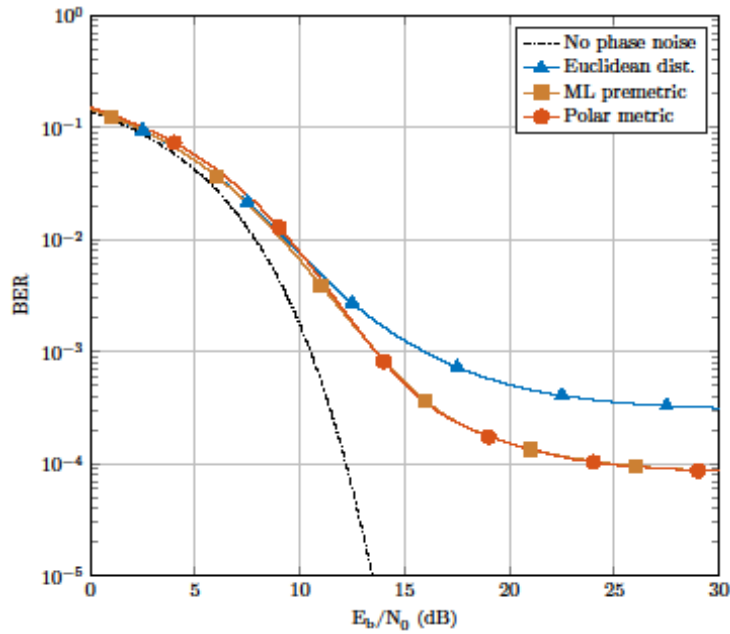


**Figure 33.1: Performance of the different decision rules for an uncoded 16-QAM with PN variance of .01**

We depict in Fig. 4.1 the BER performance of an uncoded 16-QAM with detection based either on the Euclidean distance, or on the ML premetric, or on the polar metric. First, it should be highlighted that the error floor, due to PN, is significantly reduced by using an appropriate decision rule. These simulations also demonstrate that performance achieved by the polar metric, with a simpler expression, are identical to the ML premetric one at high SNR. Fig. 4.1 is an illustration of the performance maximization through Channel-State-Information (CSI) capitalization. It is worth mentioning that using channel statistics to properly represent the signal and hence optimize the communication performance is a well-known scheme, implemented for instance in the Orthogonal Time Frequency Space (OTFS) waveform [38].

## 4.4 Probabilistic Demapper

Channel coding is indivisible of modern communication systems, for it provides a means to achieve robust communications over noisy channels. Furthermore, it is usually complemented with soft decision decoding, which is known to improve significantly the performance of channel decoders. Namely, soft decision decoding exploits the reliability information of the encoded bits. Nevertheless, it may be too complex for practical systems to evaluate directly the exact values of a probabilistic demapper. Still, they can be closely approximated in order to be efficiently computed.

### 4.4.1 Bit LLR (Log Likelihood Ratio) values

Let us here consider a Bit-Interleaved-Coded-Modulation (BICM) architecture such that the symbol  $s$  maps the binary word  $\mathbf{b} = (b_1, \dots, b_{\log_2 M})$ . The optimum hard decision on the simple detection problem regarding bit  $b_i$  is achieved by the ML criterion [37]

$$\hat{b}_i(r) = 1, \quad \text{if } L_i(r) > 0 \quad (4.14)$$

$$\hat{b}_i(r) = 0, \quad \text{otherwise}$$

where  $L_i$ , the Log-Likelihood-Ratio (LLR) of decision  $\hat{b}_i(r)$ , is defined by

$$L_{i(r)} = \log \left( \frac{p(b_i = 1|r)}{p(b_i = 0|r)} \right). \quad (4.14)$$

While the sign of the LLR supplies the decision to be taken, its absolute value quantifies the reliability of this decision. By applying Bayes' rule and assuming equiprobable symbols, the LLR may be written as

$$L_i(r) = \log \left( \frac{\sum_{s_1 \in C_1^i} p(r|s_1)}{\sum_{s_0 \in C_0^i} p(r|s_0)} \right), \quad (4.15)$$

where  $C_\beta^i$  denote the subset of the constellation symbols satisfying  $b_i = \beta$ . This expression are tedious to evaluate directly. However, simplified but suboptimal LLR can be obtained through the commonly used *max-log sum* approximation [39], viz.  $\log(\sum_k x_k) \simeq \max_k \log x_k$ . This approximation is tight at high SNR and leads to

$$L_i(r) \simeq \max_{s_1 \in C_1^i} \log(p(r|s_1)) - \max_{s_0 \in C_0^i} \log(p(r|s_0)). \quad (4.16)$$

In addition, most of implemented decoder algorithms are not sensitive to normalization, *e.g.* the *min-sum* decoder for LDPC. Such that, we can express the LLR upon the polar metric defined in Eq. (4.10) by

$$L_i(r) \simeq \min_{s_0 \in C_0^i} d_\gamma^2(r, s_0) - \min_{s_1 \in C_1^i} d_\gamma^2(r, s_1). \quad (4.17)$$

Several comments should be pointed out. First, this expression is identical to the LLR of an AWGN channel if  $d$  denoted the Euclidean distance [39]. Furthermore, the bit LLR values in Eq. (4.17) can be computed simply - which is not the case for the ML premetric - since the polar metric  $d_\gamma$  is no more than a weighted Euclidean distance within  $p_2$ . Although the proposed demodulation is applied to QAM constellation in the following, it is valid for any modulation scheme.

#### 4.4.2 Application: demodulation of LDPC coded $M$ -QAM

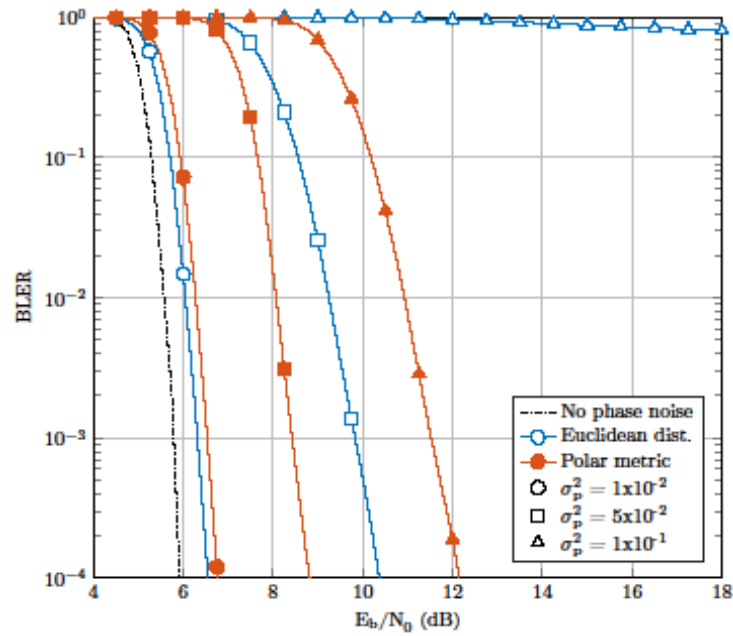


**Figure 4.2: Comparison of a LDPC coded 16-QAM performance exploiting LLR based either upon the Euclidean distance or on the polar metric for different values of PN variance**

To the best of our knowledge, performance gains provided by an appropriate decision metric for demodulation of coded systems over the Gaussian PN channel have never been evaluated. Besides, in the high-rate communications context, Low-Density-Parity-Check (LDPC) codes are recognized as a foremost solution for error-correcting codes. Due to their excellent performance and highly parallelizable decoders, they have been adopted in several recent communication standards, *e.g.* 5G-NR [40]. Therefore, a LDPC code appears as the most sensible choice to evaluate the proposed LLR expression. To be specific, the implemented code follows the specifications of the IEEE 802.11 standard [41] with a min-sum decoder, a block length of 1944 bits and a coding rate of 2/3. Fig. 4.2 presents the BLock Error Rate (BLER) performance of a 16-QAM for arbitrary values of PN variance. In particular, it is shown that the polar metric yields significant gain in performance compared to the Euclidean distance. If the SNR is low and the PN variance is minor, then the Euclidean detector slightly outperforms ( $< 0.1$  dB) the polar metric demodulation - as expected since the polar metric relies on the high SNR assumption. Yet, as PN gets stronger, the performance gain becomes more and more significant. Eventually for strong PN scenarios, the polar metric is the only one exhibiting the waterfall feature of LDPC, while the iterative decoder never converges with the Euclidean distance. Performance of the ML premetric are not shown as they are strictly identical to the ones of the polar metric, even though they are more complex to evaluate.

#### 4.5 Channel estimation for Optimal Demodulation

In previous sections, it has been emphasized that knowledge of the CSI is highly valuable to maximize the performance of communication systems affected by PN. Conversely to the Euclidean distance, the ML premetric and the polar metric are directly defined upon the thermal and phase noise variances. Greatly improving the performance, both decisions rules hence require an estimation of the values  $\sigma_n^2$  and  $\sigma_p^2$ .



#### 4.5.1 Thermal and phase noise variances estimation

Estimation of thermal and phase noise variances  $\sigma_n^2$ ,  $\sigma_p^2$  can be performed by transmitting  $N$  pilot symbols. These pilot samples are known from the receiver and denoted  $\mathbf{s} = (s_1, s_2, \dots, s_N)$ . The joint likelihood function may be derived from Eq. (4.7) and is expressed by

$$p_N(\mathbf{r}|\mathbf{s}, \sigma_n^2, \sigma_p^2) = \prod_{k=1}^{(N)} p(r_k|s_k, \sigma_n^2, \sigma_p^2), \quad (4.18)$$

where  $\mathbf{r} = (r_1, \dots, r_N)$  stands for the received samples. We consider in the following that pilots have a constant amplitude -the average symbol energy  $E_s$  is considered perfectly known as it can be estimated blindly through all sent symbols - of  $\sqrt{E_s}$ . The ML estimate [37] of the covariance matrix yields the ML estimators expressed by

$$\begin{aligned} \hat{\sigma}_n^2 &= \frac{1}{N} \sum_{k=1}^N (r_{\rho,k} - \sqrt{E_s})^2, \quad (4.19) \\ \hat{\sigma}_p^2 &= \frac{1}{N} \sum_{k=1}^N (r_{\theta,k} - s_{\theta,k})^2 - \frac{\hat{\sigma}_n^2}{E_s}. \end{aligned}$$

We can write such estimators as  $\chi^{2N}$  distributions to quantify their bias and dispersion from the means and variances:

$$E[\hat{\sigma}_n^2] = \sigma_n^2 \quad (4.20)$$

$$V[\hat{\sigma}_n^2] = \frac{2\sigma_n^4}{N}$$

$$E[\hat{\sigma}_p^2] = \sigma_p^2$$

$$V[\hat{\sigma}_p^2] = \frac{2\left(\sigma_p^2 + \frac{\sigma_n^2}{E_s}\right)^2}{N}.$$

Both of these estimators are unbiased. Therefore, it is relevant to compare their dispersions to the Cramer-Rao Lower Bounds (CRLB) [37]. Since Eq. (4.18) satisfies the regularity conditions, the CRLBs are given by

$$V[\hat{\sigma}_n^2] \geq \frac{2\sigma_n^4}{N}, \quad V[\hat{\sigma}_p^2] \geq \frac{2(\sigma_n^2 + \sigma_n^2/E_s)^2}{N}, \quad (4.21)$$

Since the variance of  $\hat{\sigma}_n^2$  equals the CRLB, the estimator is efficient *cf.* [37]. Regarding the PN variance, the estimator  $\hat{\sigma}_p^2$  is close to the CRLB but does not perfectly achieve it. Still, both estimators demonstrate the smallest Mean Square Error (MSE) among any unbiased estimator. From Eq. (4.18), it is straightforward that the joint density  $p_N$  belongs to the exponential family such that  $T = \left(\sum_{k=1}^N (r_{\rho,k} - \sqrt{E_s})^2, \sum_{k=1}^N (r_{\theta,k} - s_{\theta,k})^2\right)$  is a complete sufficient statistic for parameter  $(\sigma_n^2, \sigma_p^2)$ . By the Lehman-

Scheffé theorem, the unbiased estimators  $(\hat{\sigma}_n^2, \hat{\sigma}_p^2)$ , defined upon  $T$ , are respectively the unique Minimum-Variance Unbiased Estimators (MVUE) of  $\sigma_n^2$  and  $\sigma_p^2$ .

#### 4.6 Conclusion

In this work, we have addressed the problem of demodulation in the presence of PN. We have assumed a high SNR and a Gaussian PN to derive the optimum symbol detection decision rule. This ML decision premetric significantly reduces the BER error floor due to PN. Besides, it is possible to define a simpler metric, entitled polar metric, upon this decision rule without any loss in performance. Thereupon, we have proposed a framework to properly represent signals upon the Gaussian PN channel. Further, computable probabilistic demapper values have been defined upon the polar metric, which is not direct from the ML premetric. It has been shown that the polar metric, in comparison to the Euclidean distance, greatly enhances performance of coded systems. Since optimum demodulation requires the knowledge of CSI, we have proposed ML estimates of the thermal and phase noise variances. It is also worth mentioning that these results could be extended to lower frequency applications and Rayleigh fading channels.

## 5 Conclusion

This document is the first BRAVE deliverable that provides technical research outcomes. It is focussed on the characterization and enhanced modelling of the sub-THz physical layer, which are key requirements for the later elaboration, calibration, evaluation and demonstration of beyond-5G waveforms and modulation schemes.

A ray-based wireless channel model is extended to frequencies 90–200 GHz, and used for statistical analysis of the in-office and outdoor xhaul scenarios. Preliminary results are reported here. The simulations complexity will be increased in future work by e.g. considering furniture, bodies and MIMO.

A realistic phase noise model is proposed that applies to high-frequencies and considers the oscillator spectral properties, e.g. obtained from measurement. This will be later exploited for an accurate evaluation of communication system performance, and understand how phase noise precisely affect the detection errors.

A first sub-THz M-QAM modulation–demodulation scheme, which is based on polar metrics, is described in this document. Its greater performance compared to traditional schemes is demonstrated, and required signal processing is discussed.

The research on the physical layer modelling, waveform definition, and adequate signal processing, will be continued in frame of BRAVE work-package 2. This document is a preliminary outcome that will be completed with final results in Deliverable D2.1 due in 2020.

## References

- [1] BRAVE, *Deliverable D1.0, Beyond-5G Wireless Tbps Scenarios and Requirements*, December 2018.
- [2] ITU-R P.676-11, *Attenuation by atmospheric gases*, September 2016.
- [3] ITU-R P.838-3, *Specific attenuation model for rain for use in prediction methods*, March 2005.
- [4] ITU-R P.833-9, *Attenuation in vegetation*, September 2016.
- [5] ITU-R P.2109-0, *Prediction of building entry loss*, June 2017.
- [6] H. Zhao et al., “28 GHz millimeter wave cellular communication measurements or reflection and penetration loss in and around buildings in New York city”, in 2013 IEEE International Conference on Communications (ICC), June 2013, pp. 5163–5167.
- [7] J. Ryan, G. R. MacCartney, Jr., and T. S. Rappaport, “Indoor Office Wideband Penetration Loss Measurements at 73 GHz”, in IEEE International Conference on Communications Workshop, May 2017, pp. 1–6.
- [8] Xing Y., Rappaport T.S., “Propagation Measurement System and Approach at 140 GHz-Moving to 6G and Above 100 GHz”, 2018 IEEE Global Communications Conference (GLOBECOM), Abu Dhabi, UAE, Dec. 2018.
- [9] ITU-R P.1238-9, *Propagation data and prediction methods for the planning of indoor radiocommunication systems and radio local area networks in the frequency range 300 MHz to 100 GHz*, June 2017.
- [10] ITU-R P.1411-9, *Propagation data and prediction methods for the planning of short-range outdoor radiocommunication systems and radio local area networks in the frequency range 300 MHz to 100 GHz*, June 2017.
- [11] S. Nguyen, J. Jarvelainen, A. Karttunen, K. Haneda and J. Putkonen, “Comparing Radio Propagation Channels Between 28 and 140 GHz Bands in a Shopping Mall”, in the Proc. of the 12th European Conference on Antennas and Propagation (EuCAP), London, UK, April 2018.
- [12] L. Pometcu and R. D’Errico, “Characterization of sub-THz and mmWave Propagation Channel for Indoor Scenarios”, in the Proc. of the 12th European Conference on Antennas and Propagation (EuCAP), London, UK, April 2018.
- [13] S. Nguyen, J. Medbo, M. Peter, A. Karttunen, K. Haneda, A. Bamba, R. D’Errico, N. Iqbal, C. Diakhate and J.M. Conrat, “On the Frequency Dependency of Radio Channel’s Delay Spread: Analyses and Findings From mmMAGIC Multi-frequency Channel Sounding”, in the Proc. of the 12th European Conference on Antennas and Propagation (EuCAP), London, UK, April 2018.
- [14] Y. Corre, T. Tenoux, J. Stéphan, F. Letourneux and Y. Lostanlen, “Analysis of Outdoor Propagation and Multi-Cell Coverage from Ray-Based Simulations in sub-6GHz and mmWave Bands”, 10th European Conference on Antennas and Propagation (EuCAP), Davos, Switzerland, April 2016.

- [15] ITU-R P2040-1, *Effects of building materials and structures on radiowave propagation above about 100 MHz*, July 2015.
- [16] Y. Corre, R. Charbonnier, M. Z. Aslam and Y. Lostanlen, “Assessing the Performance of a 60 GHz Dense Small-Cell Network Deployment from Ray-Based Simulations”, IEEE CAMAD 2016, Toronto, Canada, Oct 2016.
- [17] P. Agyapong, V. Braun, M. Fallgren et al., *Simulation guidelines*, ICT METIS, Deliverable D6.1, October 2013.
- [18] A. J. Viterbi, *Principles of Coherent Communication*, McGraw-Hill Company, 1966. [Online]. Available: <https://archive.org/details/PrinciplesOfCoherentCommunicationsAndrewVeterbi>.
- [19] A. Hajimiri and T. H. Lee, “A general theory of phase noise in electrical oscillators,” IEEE Journal of Solid-State Circuits, vol. 33, no. 2, pp. 179–194, Feb 1998. [Online]. Available: <http://ieeexplore.ieee.org/document/658619/?reload=true>.
- [20] A. Demir, “Computing timing jitter from phase noise spectra for oscillators and phase-locked loops with white and  $1/f$  noise,” IEEE Transactions on Circuits and Systems I: Regular Papers, vol. 53, no. 9, pp. 1869–1884, Sept 2006. [Online]. Available: <http://ieeexplore.ieee.org/document/1703773>.
- [21] A. Chorti and M. Brookes, “A Spectral Model for RF Oscillators With Power-Law Phase Noise,” IEEE Transactions on Circuits and Systems I: Regular Papers, vol. 53, no. 9, pp. 1989–1999, Sept 2006. [Online]. Available: <http://ieeexplore.ieee.org/document/1703784/>.
- [22] M. R. Khanzadi, D. Kuylenstierna, A. Panahi, T. Eriksson, and H. Zirath, “Calculation of the performance of communication systems from measured oscillator phase noise,” IEEE Transactions on Circuits and Systems I: Regular Papers, vol. 61, no. 5, pp. 1553–1565, May 2014. [Online]. Available: <http://ieeexplore.ieee.org/document/6693756/>.
- [23] M. Voicu, D. Pepe, and D. Zito, “Performance and trends in millimetre-wave CMOS oscillators for emerging wireless applications,” International Journal of Microwave Science and Technology, vol. 2013, p. 6, 2013. [Online]. Available: <http://dx.doi.org/10.1155/2013/312618>.
- [24] R. Krishnan, A. G. i Amat, T. Eriksson, and G. Colavolpe, “Constellation optimization in the presence of strong phase noise,” IEEE Transactions on Communications, vol. 61, no. 12, pp. 5056–5066, December 2013. [Online]. Available: <http://ieeexplore.ieee.org/document/6648358/>.
- [25] D. B. Leeson, “A simple model of feedback oscillator noise spectrum,” Proceedings of the IEEE, vol. 54, no. 2, pp. 329–330, Feb 1966. [Online]. Available: <http://ieeexplore.ieee.org/document/1446612>.
- [26] R. Khanzadi, *Phase noise in communication systems : Modeling, compensation, and performance analysis*, Ph.D. dissertation, Chalmers University of Technology, 2015. [Online]. Available: <http://publications.lib.chalmers.se/records/fulltext/224284/224284.pdf>.
- [27] M. Stoisiek and D. Wolf, “Recent investigations on the stationarity of  $1/f$  noise,” Journal of Applied Physics, vol. 47, no. 1, pp. 362–364, 1976. [Online]. Available: <https://doi.org/10.1063/1.322327>.

- [28] E. Milotti, “1/f noise: a pedagogical review,” arXiv preprint physics/0204033, Apr. 2002. [Online]. Available: <https://arxiv.org/abs/physics/0204033>.
- [29] L. Barletta and G. Kramer, “On continuous-time white phase noise channels,” in IEEE International Symposium on Information Theory, June 2014, pp. 2426–2429. [Online]. Available: <http://ieeexplore.ieee.org/abstract/document/6875269/>.
- [30] H. Ghozlan and G. Kramer, “Multi-sample receivers increase information rates for wiener phase noise channels,” in 2013 IEEE Global Communications Conference (GLOBECOM), Dec 2013, pp. 1897–1902. [Online]. Available: <http://ieeexplore.ieee.org/abstract/document/6831351/>.
- [31] A. Lapidoth, “On phase noise channels at high snr,” in Proceedings of the IEEE Information Theory Workshop, Oct 2002, pp. 1–4. [Online]. Available: <http://ieeexplore.ieee.org/document/1115399/>.
- [32] N. J. Kasdin and T. Walter, “Discrete simulation of power law noise [for oscillator stability evaluation],” in Proceedings of the 1992 IEEE Frequency Control Symposium, May 1992, pp. 274–283. [Online]. Available: <http://ieeexplore.ieee.org/document/270003/Conclusion>.
- [33] M. Voicu, D. Pepe, and D. Zito, “Performance and Trends in Millimetre-Wave CMOS Oscillators for Emerging Wireless Applications,” International Journal of Microwave Science and Technology, vol. 2013, p. 6, 2013.
- [34] R. Krishnan, M. R. Khanzadi, T. Eriksson, and T. Svensson, “Soft metrics and their performance analysis for optimal data detection in the presence of strong oscillator phase noise,” CoRR, vol. abs/1310.1638, 2013.
- [35] M. R. Khanzadi, D. Kuylenstierna, A. Panahi, T. Eriksson, and H. Zirath, “Calculation of the Performance of Communication Systems From Measured Oscillator Phase Noise,” IEEE Transactions on Circuits and Systems I: Regular Papers, vol. 61, no. 5, pp. 1553–1565, May 2014.
- [36] J. Proakis, Digital Communications 5th Edition, ser. McGraw-Hill series in electrical and computer engineering : communications and signal processing. McGraw-Hill, 2007.
- [37] T. Moon and W. Stirling, *Mathematical Methods and Algorithms for Signal Processing*, Prentice Hall, 2000.
- [38] R. Hadani, S. Rakib, M. Tsatsanis, A. Monk, A. J. Goldsmith, A. F. Molisch, and R. Calderbank, “Orthogonal Time Frequency Space Modulation,” in 2017 IEEE Wireless Communications and Networking Conference (WCNC), March 2017, pp. 1–6.
- [39] F. Tosato and P. Bisaglia, “Simplified soft-output demapper for binary interleaved COFDM with application to HIPERLAN/2,” in 2002 IEEE International Conference on Communications. Conference Proceedings. ICC 2002 (Cat. No.02CH37333), vol. 2, 2002, pp. 664–668 vol.2.
- [40] 3rd Generation Partnership Project (3GPP), *Overall Description Stage 2*, Technical Specification Group Access Network 38.300, 12 2017, 2.0.0.



[41] IEEE Computer Society, *IEEE Standard for Information technology–Local and metropolitan area networks– Specific requirements– Part 11: Wireless LAN Medium Access Control (MAC)and Physical Layer (PHY) Specifications Amendment 5: Enhancements for Higher Throughput*, IEEE Std 802.11n-2009 (Amendment to IEEE Std 802.11-2007 as amended by IEEE Std 802.11k-2008, IEEE Std 802.11r-2008, IEEE Std 802.11y-2008, and IEEE Std 802.11w-2009), pp. 1–565, Oct 2009.

## Appendix A – In-office scenario CDF results

This appendix reports the various graphs that characterize the wideband channel properties predicted in the office environment (section 2.5). The statistical distribution of horizontal emitting angular spread, horizontal arrival angular spread, delay spread and coherence bandwidth are plotted for various frequencies, visibilities (LoS or NLoS) and transmit antenna beam-width.

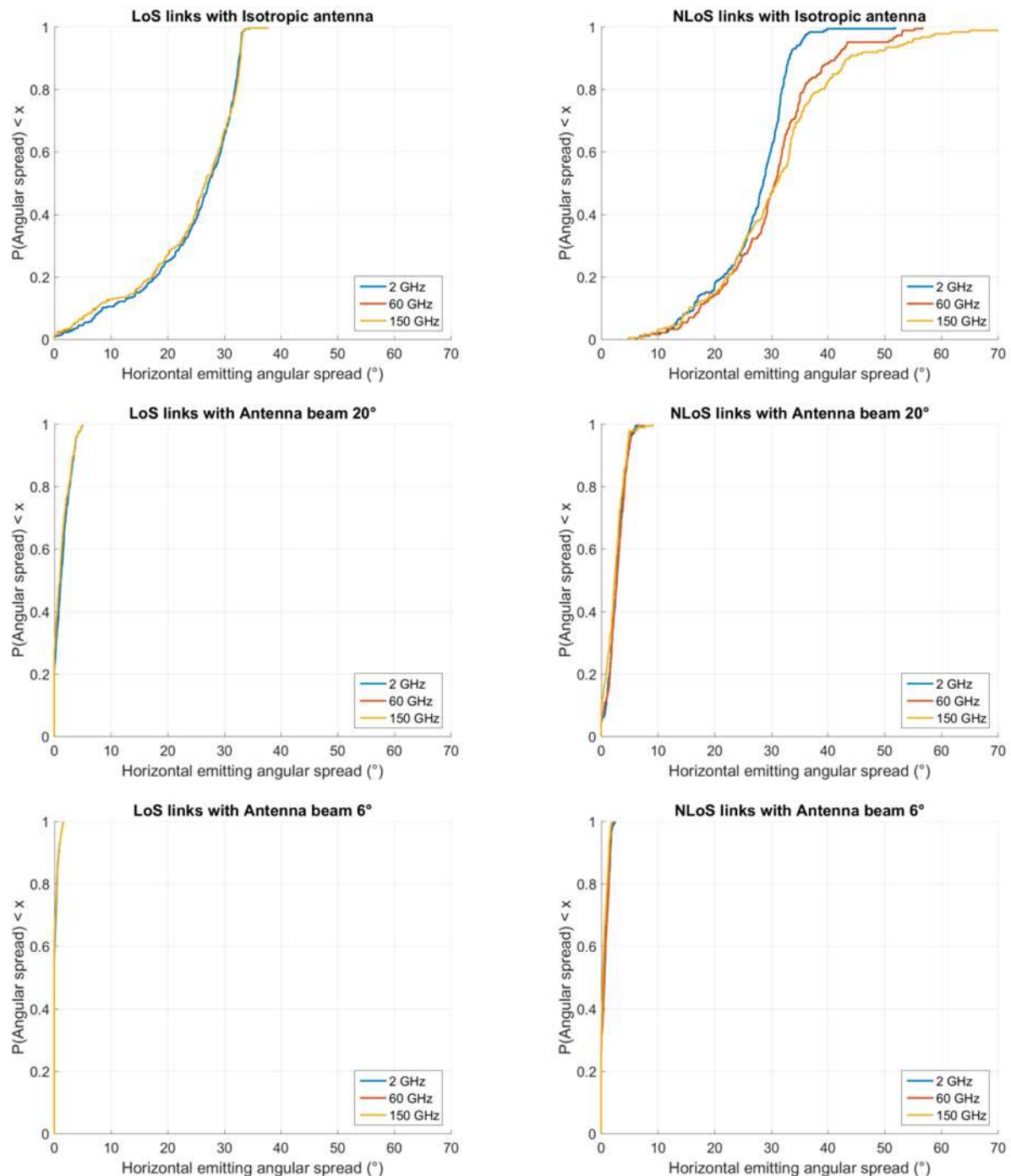


Figure 34: CDF of the horizontal emitting angular spread

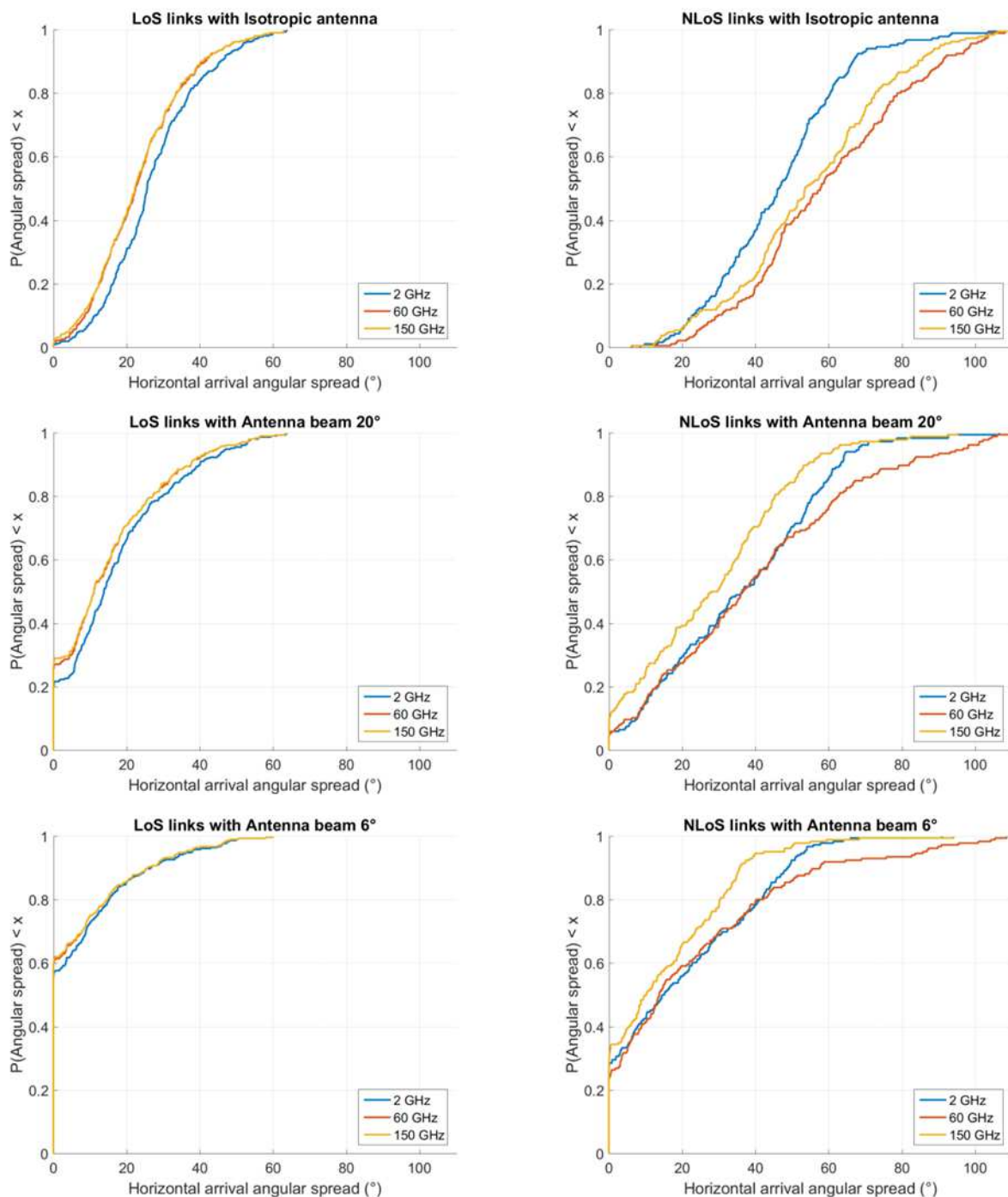


Figure 35: CDF of the horizontal arrival angular spread

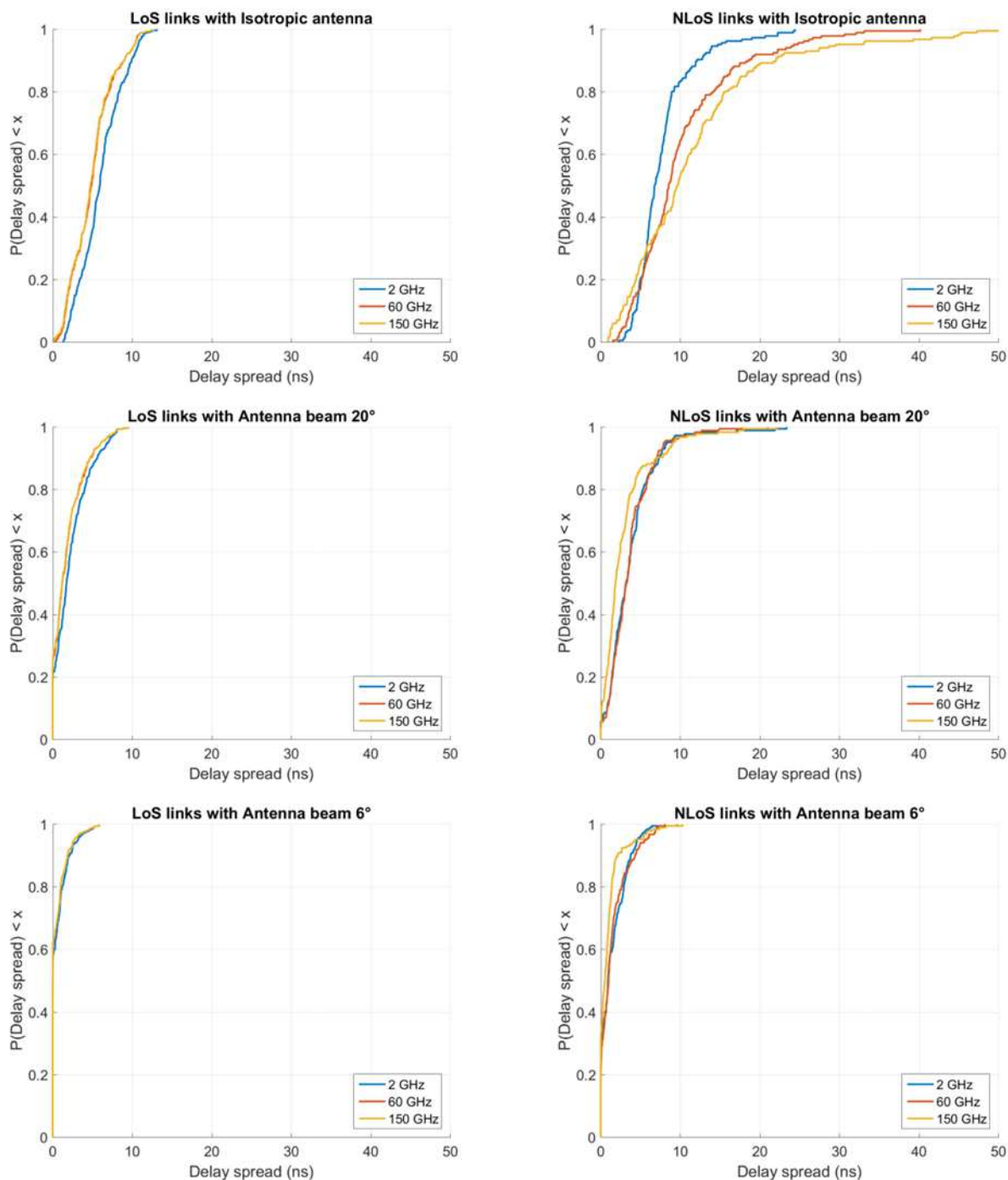


Figure 36: CDF of the delay spread

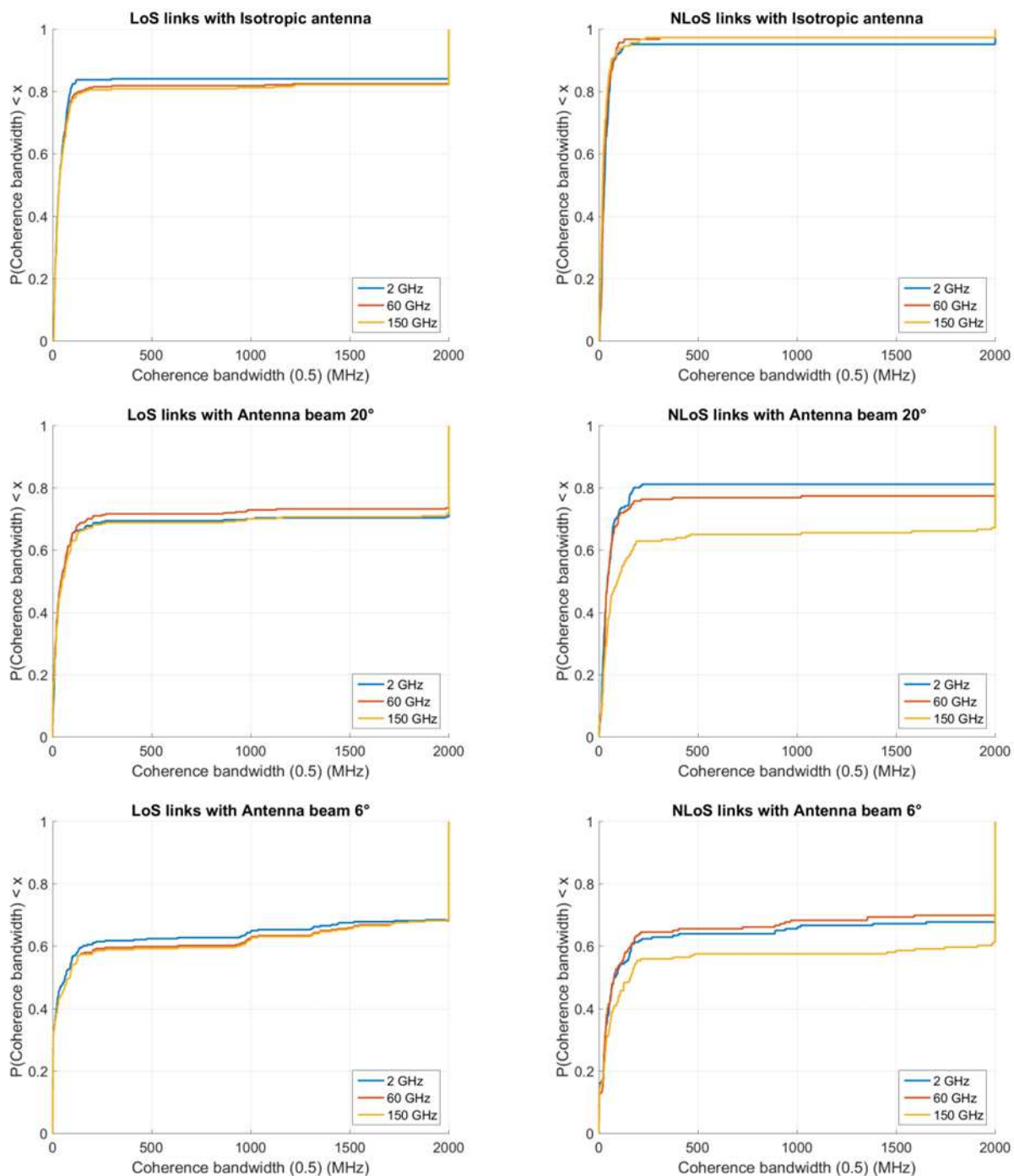


Figure 37: CDF of the coherence bandwidth